Accepted Manuscript

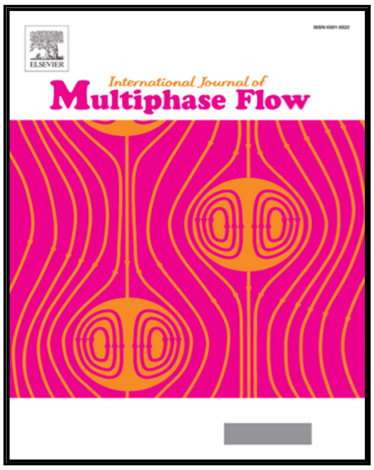

Complex wave patterns in dilute gas-particle flows based on a novel discontinuous Galerkin scheme

O. Ejtehadi , A. Rahimi , A. Karchani , R.S. Myong

PII: S0301-9322(17)30864-9
DOI: 10.1016/j.ijmultiphaseflow.2018.03.004
Reference: IJMF 2759

To appear in: *International Journal of Multiphase Flow*

Received date: 3 November 2017
Revised date: 30 January 2018
Accepted date: 3 March 2018

Please cite this article as: O. Ejtehadi , A. Rahimi , A. Karchani , R.S. Myong , Complex wave patterns in dilute gas-particle flows based on a novel discontinuous Galerkin scheme, *International Journal of Multiphase Flow* (2018), doi: 10.1016/j.ijmultiphaseflow.2018.03.004

Highlights

- Physics behind abnormal wave patterns in dusty gas flows was investigated in detail.
- DG method was for the first time applied to two-fluid model equations for gas-particle flows.
- A novel treatment of the source terms, free from assumptions of the operator splitting and zero-relaxation limit, was proposed.

Complex wave patterns in dilute gas-particle flows based on a novel discontinuous Galerkin scheme

O. Ejtehadi, A. Rahimi, A. Karchani, R.S. Myong*

School of Mechanical and Aerospace Engineering, and ACTRC & ReCAPT,
Gyeongsang National University, Jinju, Gyeongnam 52828, South Korea

*Corresponding author: Tel +82 55 772-1645 (Fax 1580); myong@gnu.ac.kr

Abstract

The present work investigates complex wave patterns in dilute gas-particle flows based on a novel discontinuous Galerkin (DG) method. For this purpose, a high order DG method was for the first time applied to two-fluid model equations for dusty gas flows. The new DG scheme not only meets the demand for high order accuracy and the positivity/monotonicity preserving property for accurately simulating dusty gas flows, but it can also handle the numerically problematic source terms efficiently, without resorting to the complicated operator splitting method commonly employed in the conventional finite volume method (FVM). For verification, several benchmark problems in one- and two-dimensional space were calculated. Special attention was then paid to the complex mechanisms of wave patterns in the dusty gas flows, which have rarely been studied in previous works, and to the physical justifications of such abnormal behaviors. In particular, it was shown that when a dust contact discontinuity is present in the flow, a pseudo-compound wave (a reflected shock attached to the rarefaction wave) as well as a composite wave (a contact discontinuity attached to the relaxation zone) can form.

Keywords: dusty gas, supersonic multiphase flow, composite wave, discontinuous Galerkin, Eulerian-Eulerian

1. Introduction

A class of multi-phase flows, composed of compressible gases carrying a substantial amount of small particles like dust or droplets, has emerged as an interesting topic in recent years. That interest is largely driven by the increasing need to understand technological processes (e.g., explosions in coal mines (Sapko et al., 2000), the separation of particulate matter from fluids (Wan et al., 2008), and the interaction of rocket plumes and lunar dust (Metzger et al., 2011)) and natural geophysical phenomena (e.g., volcanic eruptions (Walker, 1981), cosmic explosions (Popel and Gisko, 2006), and star formation (Kührt and Keller, 1996)), as summarized in Fig. 1.

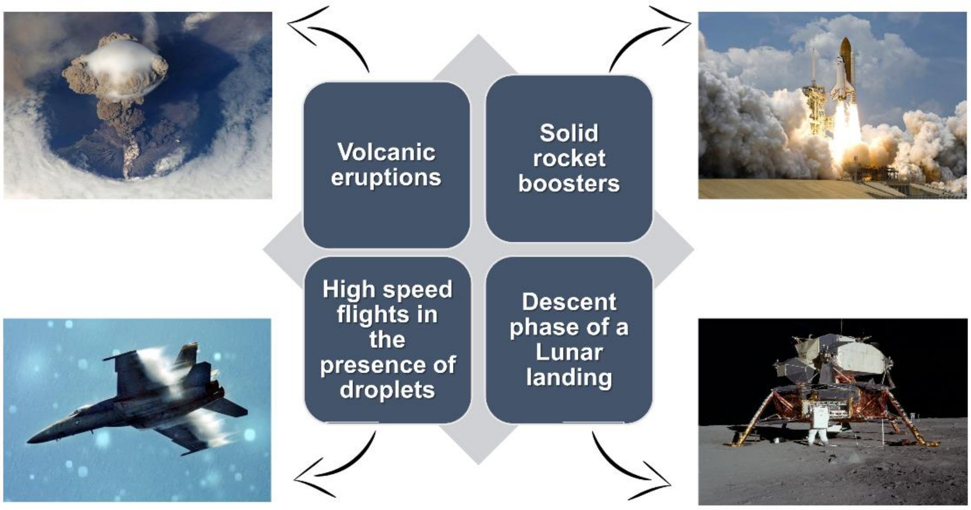

Fig. 1 Various applications of dusty gas flows

The dynamics of dusty gas flows is known to be significantly different from those of pure gas flows. This difference is essentially caused by the mass, momentum and heat exchange that occurs between the two phases. In dusty gas flows with shock waves, such as coal mine explosions or the interaction of the lunar lander's rocket plume with the dusty surface of the moon during the descent phase, there is a transition region where the velocity of the shock wave continuously changes due to the inertia and the heat capacity of the particles. Moreover, the mass exchange effects as a result of phase change or chemical reactions is important in many applications (Marble, 1970). Such complexities have motivated various theoretical (Rudinger, 1964; Satofuka and Tokita, 1979) and experimental (Lock, 1994; Sommerfeld, 1985) studies. However, most of these studies have mainly focused on the one-dimensional shock tube problem in order to obtain a comprehensive physical understanding of the dusty gas flows, and consequently development of proper mathematical models.

From a theoretical point of view, there are two prevailing approaches for predicting the dispersed flows: the trajectory (discrete or Lagrangian) and two-fluid (Eulerian-Eulerian) models (Brennen, 2005). In the trajectory model, the dispersed phase is described in the Lagrangian framework, while in the two-fluid model the dispersed phase is treated as a continuum. In the present study, the two-fluid model is preferred over the trajectory model, since it is not only applicable to a wide spectrum of particulate loading in multi-phase regimes, but also incur a less computational cost, compared to the Lagrangian counterpart. The model is, however, not efficient when the distribution of particle size is the main interest, since a separate set of equations should be solved for each diameter size.

While most of the theoretical research has been limited to the one-dimensional numerical problem (Igra et al., 1985; Miura and Glass, 1982; Sainsaulieu, 1995; Tiselj and Petelin, 1997; Toumi and Kumbaro, 1996), many recent studies have focused on developing multi-dimensional numerical tools with the capability of handling unstructured grids. Saito (2002); (Saito et al., 2003) developed a two-dimensional numerical tool to solve the two systems of conservation laws using the finite volume method. Igra et al. (1999) investigated shock wave reflection from a wedge in a dusty gas flow by using a second order accurate scheme in a finite difference framework based on the generalized Riemann problem and dimensional splitting. Moreover, they conducted an extensive parametric study on particle size and mass loading in two different time steps. In another attempt, Igra et al. (2004) extensively studied shock wave reflection from a wedge placed in various suspensions by using a finite volume method of a two-fluid model.

On the other hand, Volkov et al. (2005) solved the viscous two-phase gas-particle flow over a blunt body using an Eulerian-Lagrangian approach and investigated the effects of inter-particle collisions and two-way coupling. Pelanti and LeVeque (2006) developed the fractional step method in the finite volume framework and applied the method to the one-dimensional shock tube and two-dimensional volcanic eruption problems. Gurris et al. (2010) solved the two-fluid model of dusty gas flows with a high-resolution finite element method along with a TVD type limiter, and Douglas-Rachford splitting method to handle the source terms. Recently, Carcano et al. (2013) solved the problem of jet decomposition in both two and three dimensions using a second-order accurate semi-implicit finite volume method. In another work, Carcano et al. (2014) extensively investigated the grain-size distribution on the dynamics of under-expanded volcanic jets. Vié et al. (2016) analyzed the capability of the Eulerian moment method for solving two-way coupled particle-laden turbulent flow systems.

Although considerable research has been devoted to the problem of dusty gas flows, rather less attention has been paid to the application of high order methods to this category. Furthermore, the inefficiency of the standard numerical methods, such as finite volume or finite element methods in the presence of large source terms or highly heterogeneous porous mediums with full permeability tensors, has driven the need for new methods which can be extended to higher orders with minimal effort (Klieber and Rivière, 2006).

When small particles are present in a carrier phase, the dominance and stiffness of the source terms deteriorates the stability restrictions of an explicit numerical scheme. In implicit schemes, this effect, associated with the source terms, can also severely slow the convergence, even though the stability of the method may not be an issue. Previous studies have circumvented this problem by using a multiple-time stepping scheme, i.e., splitting of the system of equations into stiff and non-stiff terms. However, the classical splitting schemes tend to reduce the order of accuracy or increase the computational cost in the best-case scenario (Gosse, 2000; LeVeque and Yee, 1990). Moreover, previous studies using the Particle-In-Cell (PIC) method (Levine, 1971) and the finite difference method (Satofuka and Tokita, 1979) on simulations of a shock wave incident into a dusty gas flow have reported a severe smearing of the shock wave due to numerical artifacts. However, the recent developments demonstrate that PIC methods can provide promising results in this class of problems (Jacobs and Don, 2009; McFarland et al., 2016).

The long-term goal of the present study is to investigate the impingement of the rocket plume on the lunar surface and the subsequent dusty gas flows formed by ejection of solid particles from the regolith during the descent phase of the lunar lander (Metzger et al., 2011). A schematic of the problem is illustrated in Fig. 2. The multi-scale nature of the physical phenomena in this problem leads to a coexistence of various flow regimes, which makes the numerical simulation extremely challenging (Tosh et al., 2011). As the first step toward this goal, we seek high-resolution solutions for dusty gas flows governed by an Euler type multiphase system of equations in the framework of the discontinuous Galerkin (DG) method.

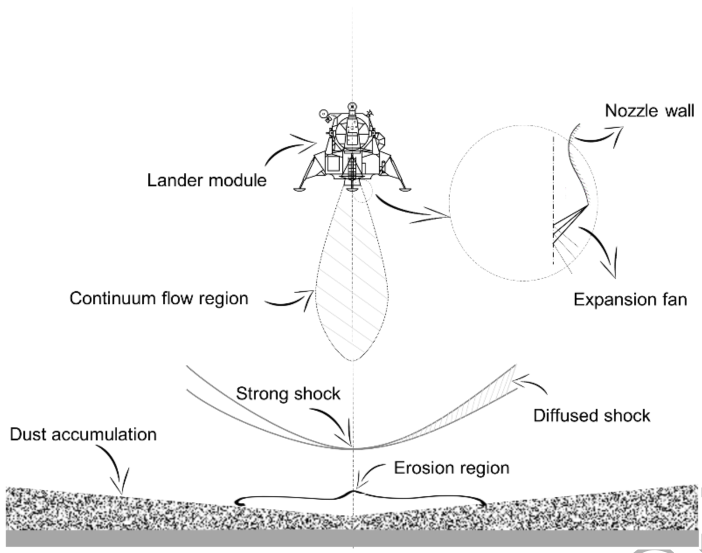

Fig. 2. Schematic of the impingement of engine plume and the subsequent dusty gas flows formed by the ejection of solid particles from the regolith during the lunar landing

First introduced by Reed and Hill (1973) and further developed by (Cockburn and Shu, 1988, 1989, 1998), the DG method has become a prominent tool for solving the fluid dynamics governing equations. While the DG method has been successfully applied to various class of problems such as compressible and incompressible flows, aeroacoustics, magneto-hydrodynamics, and many more (Cockburn et al., 2000), it has recently also found its way into the multiphase problem. This application is driven by improvement of the method, as well as recent advances in computer resources, which make the DG method a feasible tool for a larger number of industrial applications.

Franquet and Perrier (2012) developed a robust high order DG method for compressible multiphase flows based on the Baer and Nunziato type systems and reported good agreement with experimental results. They also extended the method to reactive multiphase flows (Franquet and Perrier, 2013). Owkes and Desjardins (2013) applied the DG method to conservative level set equations for interphase capturing in multiphase flows. Lu et al. (2016) presented a Runge-Kutta DG method together with the front tracking method for solving two-medium gas-gas and gas-liquid flows. de Frahan et al. (2015) obtained the DG solution for multiphase flows using the Mie-Grüneisen family of equations of state. Recently, Dumbser and Loubère (2016) proposed an accurate nonlinear a posteriori stabilization of the DG method and applied the method to the Baer-Nunziato model in two-dimensional space. Moortgat and Firoozabadi (2016) developed a vertex-based DG method of multiphase compositional flow on 3D unstructured grids. Diehl et al. (2016) obtained the solutions of the Navier-Stokes-Korteweg equations for compressible liquid-vapor multiphase flow with phase transition using the local discontinuous Galerkin (LDG) method.

Although these recent studies demonstrated the capability of the DG method for very diverse problems, few mathematical models pertaining to multiphase flow categories or regimes have been investigated using the DG method. *To the best knowledge of the authors, there is no previous work on applications of a high order DG method to solve a two-fluid model of dusty gas flows*. Further, in flow problems with strong discontinuities and the presence of stiff source terms due to the coupling effects in the two-fluid model, the mere application of high-order methods without proper treatment of numerical artifacts or without proper handling of the non-homogeneous part of the partial differential equation will generally lead to divergence, an oscillatory solution or in the best scenario a huge computational penalty, caused by small time steps.

In this study, we set out to investigate the complex mechanisms of wave patterns in dilute gas-particle flows, which were rarely studied in previous works, and the physical justification for such abnormal behaviors. In particular, it will be demonstrated that, when a contact discontinuity in dust is present in the dusty gas flow, a pseudo-compound wave as well as a composite wave can be formed.

To this end, the mathematical model of the gas and solid phases and a novel modal unstructured DG method are first presented. A detailed description of the positivity and monotonicity preserving property of the new scheme then follows. Further, a novel treatment of source terms, free from the aforementioned weaknesses in conventional methods based on operator splitting and zero-relaxation limit, is highlighted. Finally, the unique features of dusty gas flows, e.g. formation of a reflected shock attached to the rarefaction wave and a contact discontinuity attached to the relaxation zone, which were not observed in pure gas flows, are identified, and a physical explanation of the origin of such abnormal waves is provided.

2. Theoretical background

In this section, the two-fluid model of dusty gas flows will be explained briefly. In what follows, the carrier phase (gas) and the dispersed phase (solid dust) are indicated by the subscripts g and s. In the Eulerian-Eulerian approach, both phases are considered continua. The gas phase is considered an inviscid and compressible flow obeying the perfect equation of state, while the dispersed phase is considered an incompressible continuum in which the particles do not collide with each other. Consequently, there is no pressure term in the conservation laws of the solid phase. The interaction of the two phases is taken into account via source terms, i.e. by momentum and heat transfer exchange between the gas and particles. Other interfacial effects including lift and gravity can be neglected, since they are small compared to drag and heat transfer.

Before describing the details of the model, some basic multiphase flow parameters are defined. The level of interaction of phases is assessed by volume fraction of the dispersed phase (α_s) and the mass loading (β). Small values of α_s and β implies that the carrier phase is not affected by the dispersed phase and the one-way coupling is satisfactory. In cases where the mass of both phases are comparable, in order to take both phases into account, the two-way coupling is necessary. For larger α_s, the particle-particle interactions such as collision, agglomeration and break-up may not be ignored, requiring a four-way coupling. The other important parameter to quantify how the phases can equilibrate is the Stokes number, defined as the ratio of aerodynamic response time of the particle (τ_s) to some characteristic time of the carrier phase (t_{ref}). Useful discussions regarding basic multiphase parameters can be found in (Balachandar and Eaton, 2010; McFarland et al., 2016).

2.1. Mathematical model of the gas and solid phases

Under the aforementioned conditions, the conservation law can be written as follows:

For the gas phase,

$$\partial_t \mathbf{U}_g + \nabla \cdot \mathbf{F}_g = \mathbf{S} \quad , \tag{1}$$

$$\mathbf{U}_g = \begin{bmatrix} \alpha_g \rho_g \\ \alpha_g \rho_g \mathbf{u}_g \\ \alpha_g \rho_g E_g \end{bmatrix}, \quad \mathbf{F}_g = \begin{bmatrix} \alpha_g \rho_g \mathbf{u}_g \\ \alpha_g \rho_g \mathbf{u}_g \mathbf{u}_g + p\mathbf{I} \\ (\alpha_g \rho_g E_g + p)\mathbf{u}_g \end{bmatrix}, \quad \mathbf{S} = \begin{bmatrix} 0 \\ D_{g,s}(\mathbf{u}_s - \mathbf{u}_g) \\ D_{g,s}(\mathbf{u}_s - \mathbf{u}_g)\mathbf{u}_s + Q_g(T_s - T_g) \end{bmatrix}, \tag{2}$$

$$E_g = c_v T_g + \frac{1}{2}\left|\mathbf{u}_g\right|^2, \tag{3}$$

and for the solid phase,

$$\partial_t \mathbf{U}_s + \nabla \cdot \mathbf{F}_s = -\mathbf{S}, \tag{4}$$

$$\mathbf{U}_s = \begin{bmatrix} \alpha_s \rho_s \\ \alpha_s \rho_s \mathbf{u}_s \\ \alpha_s \rho_s E_s \end{bmatrix}, \quad \mathbf{F}_s = \begin{bmatrix} \alpha_s \rho_s \mathbf{u}_s \\ \alpha_s \rho_s \mathbf{u}_s \mathbf{u}_s \\ (\alpha_s \rho_s E_s)\mathbf{u}_s \end{bmatrix}, \tag{5}$$

$$E_s = c_m T_p + \frac{1}{2}\left|\mathbf{u}_s\right|^2, \tag{6}$$

$$\alpha_g + \alpha_s = 1. \tag{7}$$

Here the **U**, **F** and **S** are the vectors of conservative variables, fluxes, and source terms, respectively. The variables t, α, ρ, $\mathbf{u}$, E, p, T, D and Q represent time, volume fraction, density, velocity vector, total energy, pressure, temperature, interphase drag and heat flux, respectively. The dust density ρ_s is assumed to be constant. c_v and c_m are the specific heat capacity of the gas at constant volume and the specific heat of the particle material. The equation of state expresses the gas pressure in terms of other gas properties:

$$p = \rho_g R T_g, \tag{8}$$

where R is the gas constant.

According to Miura and Glass (1982), the drag force that solid particles exert on the gas phase can be expressed as

$$D_{g,s} = \frac{3}{4} C_D \frac{\alpha_s \rho_g}{d}\left|\mathbf{u}_g - \mathbf{u}_s\right|, \tag{9}$$

in which d is the particle diameter and C_D is the drag coefficient computed as a function of the Reynolds number based on the particle diameter and relative velocity of the particle to the gas (i.e. $\mathrm{Re}_d = \frac{\rho_g d \left|\mathbf{u}_g - \mathbf{u}_s\right|}{\mu_g}$). The drag coefficient can then be given by a well-stablished semi-empirical correlation (Dobran et al., 1993),

$$C_D = \begin{cases} \frac{24}{\mathrm{Re}_d}\left(1+0.15\,\mathrm{Re}^{0.687}\right), & \text{if} \quad \mathrm{Re}<1000 \\ 0.44, & \text{if} \quad \mathrm{Re}>1000 \end{cases} \tag{10}$$

The heat transfer, which is proportional to temperature difference, can be expressed as a function of the Nusselt number (Knudsen and Katz, 1958),

$$Q_g = \frac{6\mathrm{Nu}\kappa_{\mathrm{g}}}{d^2}\alpha_s(T_g - T_s)\,, \tag{11}$$

$$\mathrm{Nu} = 2 + 0.65\,\mathrm{Re}_d^{\frac{1}{2}}\,\mathrm{Pr}^{\frac{1}{3}}\ ,\ \mathrm{Pr} = \frac{c_p\mu_g}{\kappa_g}\,. \tag{12}$$

Here μ_g and κ_g represent the viscosity and thermal conductivity of the gas, respectively.

2.2. Dimensionless form of the governing equations

The following dimensionless variables and parameters are used to derive the non-dimensional governing system of equations. Here the dimensionless parameters are superscripted by * and the reference values are denoted by the subscript *ref*,

$$\begin{gathered} \mathbf{x}^* = \frac{\mathbf{x}}{L}, \quad t^* = \frac{t}{t_{ref}}, \quad \mathbf{u}^* = \frac{\mathbf{u}}{u_{ref}}, \quad T^* = \frac{T}{T_{ref}}, \quad \rho^* = \frac{\rho}{\rho_{ref}}, \quad p^* = \frac{p}{p_{ref}}, \\ E^* = \frac{E}{E_{ref}}, \quad Q^* = \frac{Q}{Q_{ref}}, \quad \mu^* = \frac{\mu}{\mu_{ref}}, \quad \kappa^* = \frac{\kappa}{\kappa_{ref}}, \\ {c_p}^* = \frac{c_p}{c_{p_{ref}}}, \quad {c_v}^* = \frac{c_v}{c_{v_{ref}}}. \end{gathered} \tag{13}$$

In the above relations, $\mathbf{x}$ and c_p are the spatial coordinates and the specific heat capacity at constant pressure, respectively. We then define the references and non-dimensional parameters as follows:

$$
\begin{gathered}
t_{ref} = \frac{L}{u_{ref}}, \quad \tau_s = \frac{\rho_s d_s^2}{18\mu} \quad E_{ref} = u_{ref}^2, \quad Q_{ref} = \frac{\kappa \Delta T_{ref}}{L}, \\
M = \frac{u_{ref}}{a_{ref}}, \quad \mathrm{Re} = \frac{\rho_{ref} u_{ref} L}{\mu_{ref}}, \quad \mathrm{Pr} = \frac{\mu_{ref} C_{p_{ref}}}{\kappa_{ref}}, \quad \mathrm{Pe} = \mathrm{Re}\,\mathrm{Pr}, \\
\gamma = \frac{C_{p_{ref}}}{C_{v_{ref}}}, \quad \frac{1}{N_\delta \mathrm{Re}} = \frac{p_{ref}}{\rho_{ref} u_{ref}^2}, \\
N_\delta = \frac{\mu_{ref} u_{ref}}{p_{ref} L}, \quad \frac{1}{\mathrm{Re}\,\mathrm{Pr}\,\mathrm{Ec}} = \frac{1}{\mathrm{Pe}} \frac{C_{p_{ref}} T_{ref}}{u_{ref}^2}, \\
St = \frac{\tau_s}{t_{ref}}, \quad Ec = \frac{u_{ref}^2}{C_{p_{ref}} T_{ref}}.
\end{gathered} \tag{14}
$$

After applying these to equations (1)-(6), the following non-dimensional system of equations can be derived:

$$
\begin{gathered}
\partial_t \mathbf{U}_g + \nabla \cdot \mathbf{F}_g = \mathbf{S} \\
\mathbf{U}_g = \begin{bmatrix} \alpha_g \rho_g \\ \alpha_g \rho_g \mathbf{u}_g \\ \alpha_g \rho_g E_g \end{bmatrix}, \quad \mathbf{F}_g = \begin{bmatrix} \alpha_g \rho_g \mathbf{u}_g \\ \alpha_g \rho_g \mathbf{u}_g \mathbf{u}_g + \dfrac{1}{N_\delta \mathrm{Re}} p\mathbf{I} \\ (\alpha_g \rho_g E_g + \dfrac{1}{N_\delta \mathrm{Re}} p)\mathbf{u}_g \end{bmatrix}, \\
\mathbf{S} = \begin{bmatrix} 0 \\ \dfrac{1}{St}(\mathbf{u}_s - \mathbf{u}_g) \\ \dfrac{1}{St}(\mathbf{u}_s - \mathbf{u}_g).\mathbf{u}_s + \dfrac{\mathrm{Nu}}{EcPe}(T_s - T_g) \end{bmatrix} \\
\partial_t \mathbf{U}_s + \nabla \cdot \mathbf{F}_s = -\mathbf{S} \\
\mathbf{U}_s = \begin{bmatrix} \alpha_s \rho_s \\ \alpha_s \rho_s \mathbf{u}_s \\ \alpha_s \rho_s E_s \end{bmatrix}, \quad \mathbf{F}_s = \begin{bmatrix} \alpha_s \rho_s \mathbf{u}_s \\ \alpha_s \rho_s \mathbf{u}_s \mathbf{u}_s \\ (\alpha_s \rho_s E_s)\mathbf{u}_s \end{bmatrix}
\end{gathered} \tag{15}
$$

Here the superscript * has been omitted for the sake of simplicity. The reference values for the length, pressure, temperature and velocity, $L=4\rho_s d/(3\rho_{ref})$, p_{ref}=1 atm, T_{ref}=273.15 K, and u_{ref}= 331.41 m/s, respectively, are employed in all simulations.

3. Numerical framework based on a modal unstructured discontinuous Galerkin method

The equations of the dusty gas flows described in the previous section are discretized using a modal discontinuous Galerkin (DG) method. The essential parts of the modal unstructured DG method developed in the present work—in particular, high order accuracy and positivity/monotonicity preserving property—are summarized in this section. For a more detailed discussion on general DG methods, readers are referred to (Cockburn et al., 2000; Cockburn and Shu, 1988, 1989, 1998), (Cockburn et al., 2000; Cockburn and Shu, 1988, 1989, 1998) for DG implementations, and Barth and Jespersen (1989); (Kontzialis and Ekaterinaris, 2013; Wang et al., 2012; Zhang and Shu, 2010b) for limiter-related issues.

3.1. A modal DG formulation

The mathematical model of interest in the present work can be written in a compact form;

$$\partial_t \mathbf{U} + \nabla \cdot \mathbf{F}(\mathbf{U}) = \mathbf{S}(\mathbf{U}) \qquad \text{in} \left[(t,\Omega) \middle| t \in (0,\infty), \Omega \subset \square \right], \tag{16}$$

where Ω denotes a bounded domain, and **U**, **F**, **S** are conservative variables vector, flux tensor, and source terms vector, respectively. The solution domain can be decomposed by a group of non-overlapping elements, $\Omega = \Omega_1 \cup \Omega_2 \cup \ldots \Omega_{ne}$, in which *ne* is the number of elements. By multiplying a weighting function φ_i into the conservative laws (16) and integrating over the control volume for each element, the following formulation can be derived:

$$\int_{\Omega_k} \left[\partial_t \mathbf{U} \varphi(\mathbf{x}) + \nabla \cdot F(\mathbf{U}) \varphi(\mathbf{x}) - S(\mathbf{U}) \varphi(\mathbf{x}) \right] d\Omega = 0 \,. \tag{17}$$

In order to construct a discretized system of the conservation laws, the global spatial domain Ω can be approximated by Ω_h where, $\Omega_h \rightarrow \Omega$ as $h \rightarrow 0$. The approximated domain, which is a tessellation of the space by bounded elementary control volumes, $\mathcal{T}_h = \{\mathbf{\Omega}_k\}$, is filled with *ne* number of the non-overlapping elements $\Omega_k \in \mathcal{T}_h$. The exact solution of the governing equations can be approximated by the numerical solution in every local element as

$$\mathbf{U}(\mathbf{x},t) \approx \mathbf{U}_h = \sum_{e=1}^{ne} \mathbf{U}_h^e(\mathbf{x},t) \equiv \mathbf{U}_h^1 + \ldots + \mathbf{U}_h^n \,. \tag{18}$$

By splitting the integral over Ω_h into series of the integrals over the sub-elements and applying the integration by part as well as divergence theorem to the equation (17), the elemental formulation reads as

$$\begin{aligned} &\int_{\Omega_k} \partial_t \mathbf{U}_h \varphi_i(\mathbf{x}) \mathrm{d}\Omega_k + \oint_{\partial\Omega_k} \varphi_i(\mathbf{x}) \mathbf{F}(\mathbf{U}_h) \cdot \hat{n} d\sigma - \int_{\Omega_k} \nabla \varphi_i(\mathbf{x}) \cdot \mathbf{F}(\mathbf{U}_h) \mathrm{d}\Omega_k \\ &= \int_{\Omega_k} \varphi_i(\mathbf{x}) \mathbf{S}(\mathbf{U}_h) \mathrm{d}\Omega_k \end{aligned} \,, \tag{19}$$

where $\hat{n}$ is the outward normal vector of the element interface and $\mathbf{U}_h$ is the *p*-exact polynomial approximated solutions of the $\mathbf{U}$ on the discretized domain of Ω_h. $\mathbf{U}_h$ can be expressed as the polynomial field that sums the multiplication of local degree of freedom with the corresponding smooth polynomials of degree P in the standard element:

$$\mathbf{U}_h = \sum_{i}^{P} a_i(t) \varphi_i(\mathbf{x}) \,. \tag{20}$$

Here $a_i(t)$ and $\varphi(\mathbf{x})$ denote the local degree of freedom and the basis function, which can be chosen to be any continuous polynomial function, respectively.

In the one-dimensional case, the orthogonal scaled Legendre functions were selected as basis functions, while a linear mapping function was used for mapping from the physical space to the standard element. In the two-dimensional case, the PDK polynomials (Dubiner, 1991) were selected as basis functions, while a collapsed coordinate transformation was used to transfer the triangles in the physical domain to the standard square elements, Ω_e, in which the coordinates (a, b) are bound by constant limits

$$\mathcal{R} = \{(a,b) \mid -1 \le a, b \le 1\} . \tag{21}$$

Another transformation was introduced to transfer the triangle in the physical space into the computational space where the new local coordinates have independent bounds, as depicted in Fig. 3. A suitable coordinate system, which describes the triangular region between constant independent limits, can be defined by the following inverse transformation:

$$r = \frac{(1+a)(1-b)}{2} - 1, \quad w = b . \tag{22}$$

New local coordinates (r, w) can then define the standard triangular region as follows:

$$\mathcal{T} = \{(r,w) \mid -1 \le r, w; r + w \le 0\} . \tag{23}$$

For more details on the various transformations used in the DG method, readers are referred to (Karniadakis and Sherwin, 2013).

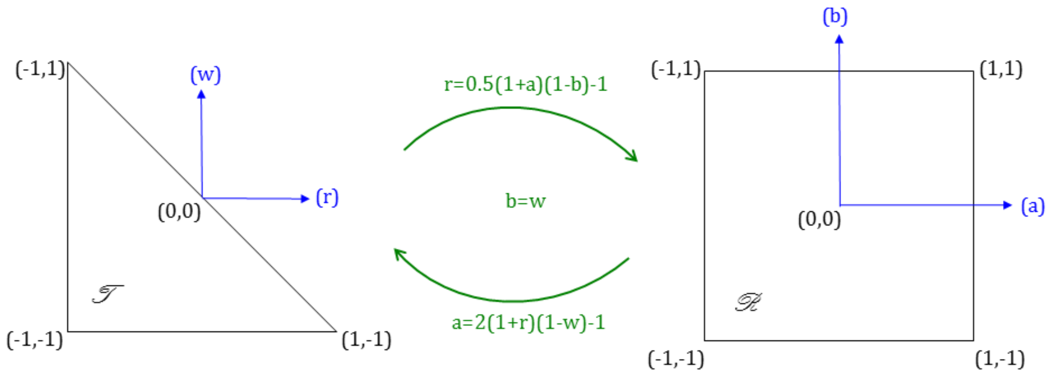

Fig. 3 Coordinate transformation

The simple and efficient local Lax-Friedrichs (LLF) flux function, commonly used in the DG method, is applied for all the multiphase test cases in the present study. Despite the dissipative nature of the numerical flux, it improves the linear stability of the DG numerical approximation. The dimensionless form of the LLF flux is defined as

$$\mathbf{F}(\mathbf{U}_h) \approx \hat{\mathrm{f}}_i\left(\mathbf{U}_h^-, \mathbf{U}_h^+\right) = \frac{1}{2}\left[\mathbf{F}_i\left(\mathbf{U}_h^-\right) + \mathbf{F}_i\left(\mathbf{U}_h^+\right) - C\left(\mathbf{U}_h^+ - \mathbf{U}_h^-\right)\right], \tag{24}$$

where C is the maximum modulus of the eigenvalues of the Jacobian matrix, $\max_{\min(U^-,U^+)\le u\le \max(U^-,U^+)} |\mathrm{F}_i'(U)|$, and for convex fluxes it reads as $C = \max\left(\left|v^-\right| + a_S^-, \left|v^+\right| + a_S^+\right)$. Here $a_S = \sqrt{T} / M$ is the speed of sound at an elemental interface, and the superscripts (+) and (–) denote the inside and outside of an elemental interface, respectively.

Moreover, a third-order accurate, third-stages total-variation-diminishing Runge-Kutta method was employed for time integration, owing to its simplicity, efficiency, and robustness. In order to minimize the temporal discretization error, the time step was set in such a way that the Courant-Friedrich-Levy (CFL) criterion is always satisfied. The Gauss-Legendre quadrature rule was used to calculate the volume and surface integrals in (19), which are proved to be 2P and 2P+1 order accurate, respectively.

3.2. Positivity preserving scheme

High order conservative schemes, including the DG scheme introduced in the previous section, usually suffer from the non-physical negative density or pressure. This situation leads to the ill-posedness of the system and numerical breakdowns in consequence. On the other hand, in the case of conservation laws with source terms which are added to account for chemical reactions, gravity or the interaction of phases, as in the present case, the possibility of encountering negative density or pressure during numerical simulation increases. Therefore, the application of an efficient positivity preserving schemes is necessary to prevent the numerical breakdown. In the present work, the positivity preserving scheme of Zhang and Shu (2011) for compressible Euler equations was applied to ensure the positivity of density and pressure fields, while maintaining the higher order accuracy.

The application of this limiter was proved to provide stable schemes for unstructured triangular meshes with favorable results (Kontzialis and Ekaterinaris, 2013). We report the first application of this type of limiter to the two-fluid model of dusty gas flows. Our numerical experiments on all the test cases show that application of a positivity preserving limiter is necessary to obtain converged solutions without compromising the accuracy of the solution.

3.3. Monotonicity preserving scheme

Our numerical investigations show that simple application of the positivity preserving scheme is not enough to develop a stable scheme, especially in the presence of strong shock waves. The situation deteriorates when the multiphase system with source terms is being solved. In the present study, the limiter of Zhang and Shu (2010a) for one-dimensional cases and the limiter of Barth and Jespersen (1989) which was initially devised for the finite volume framework are applied. It is important to note that any TVD/MUSCL type scheme can degrade the order of accuracy in the smooth regions of the solution, unless a pragmatic shock detection scheme is introduced. The detailed implementation of the scheme can be found in (Barth and Jespersen, 1989).

3.4. Boundary conditions

The implementation of boundary conditions in two-fluid or multi-fluid systems requires a different set of conditions for each phase. The benchmark problems considered in this paper are free from boundary effects, except the compression corner test case, in which an adiabatic, impermeable, inviscid wall boundary condition is applied for both phases (Kim and Chang (1991). Other boundary conditions choices like the adherence condition or reflection conditions are also viable for the solid phase (Saurel et al., 1994). When the viscous system of conservation laws (e.g. Navier-Stokes-Fourier) is considered, it is necessary to use a non-slip boundary condition for the gas phase and a slip boundary condition for the solid phase.

3.5. Novel source terms treatment

It was well-known that the stiff relaxation terms in balance laws (i.e., strictly hyperbolic systems with source terms) lead to disparate relaxation times, which in turn results in severe numerical difficulties. In the case of the two-fluid model, in addition to the time scale related to the convection, a much smaller relaxation time scale exists that inevitably imposes smaller time steps on the numerical solver. The use of a slower time scale in such problems can cause severe numerical instability.

The most well-known methods for removing this limitation are the operator splitting and zero-relaxation limit; however, as reported in Béreux (1996), the range of validity of each method is very limited, to the product of relaxation time and the acoustic wave pulsation. Moreover, spurious solutions may arise when the effects of the source terms are not properly resolved (LeVeque and Yee, 1990). Finally, it is well established that the convergence rate of the first-order finite difference methods for conservation laws will be no better than $O(h^{1/2})$ (Lucier, 1985). Here we demonstrate that the inherent feature of the new DG scheme bypasses the need to apply such inefficient treatments in conventional methods.

For a single variable u_h, the elemental formulation (19) reduces to

$$\begin{aligned}
&\frac{d}{dt}\int_{\Omega_k} u_h \varphi_i(\mathbf{x})\mathrm{d}\Omega_k + \oint_{\partial\Omega_k} F(u_h)\cdot\hat{n}\varphi_i(\mathbf{x})d\sigma - \int_{\Omega_k} F(u_h)\cdot\nabla\varphi_i(\mathbf{x})\mathrm{d}\Omega_k \\
&= \int_{\Omega_k} S(u_h)\varphi_i(\mathbf{x})\mathrm{d}\Omega_k .
\end{aligned} \tag{25}$$

Taking $\mathbf{U}$ as the global vector of degrees of freedom, this equation can be written in a matrix form:

$$\begin{aligned}
&\mathbf{M}\frac{d\mathbf{U}}{dt} - \mathbf{K}\mathbf{U} + \widehat{F}(u_h)\mathbf{\Theta} - S(u_h)\mathbf{\Theta}' = 0 \\
&\frac{d\mathbf{U}}{dt} - \mathbf{M}^{-1}\mathbf{K}\mathbf{U} + \widehat{F}(u_h)\mathbf{M}^{-1}\mathbf{\Theta} - S(u_h)\mathbf{M}^{-1}\mathbf{\Theta}' = 0 \\
&\frac{d\mathbf{U}}{dt} = L(\mathbf{U}) \\
&\mathbf{U} = (U^{(1)}, U^{(2)}, ..., U^{(N)})^T \\
&L(\mathbf{U}) = \mathbf{M}^{-1}\mathbf{K}\mathbf{U} - \widehat{F}(u_h)\mathbf{M}^{-1}\mathbf{\Theta} + S(u_h)\mathbf{M}^{-1}\mathbf{\Theta}'
\end{aligned} \tag{26}$$

Here, $\mathbf{M}$ and $\mathbf{K}$ are the mass and stiffness matrixes, and $\mathbf{\Theta}$ and $\mathbf{\Theta}'$ are the vectors that incorporate the contributions of the boundary and source terms, respectively. The matrixes are defined as follows:

$$\mathbf{M} = \int_{\Omega_k} \varphi_i(\mathbf{x})\varphi_j(\mathbf{x})\mathrm{d}\mathbf{\Omega}_k \quad \forall \quad 1 \le i \le j \le n$$
$$= \begin{bmatrix} \int_{\Omega_k} \varphi_1(\mathbf{x})\varphi_1(\mathbf{x})\mathrm{d}\mathbf{\Omega}_k & \int_{\Omega_k} \varphi_1(\mathbf{x})\varphi_2(\mathbf{x})\mathrm{d}\mathbf{\Omega}_k & \cdots & \int_{\Omega_k} \varphi_1(\mathbf{x})\varphi_n(\mathbf{x})\mathrm{d}\mathbf{\Omega}_k \\ \int_{\Omega_k} \varphi_2(\mathbf{x})\varphi_1(\mathbf{x})\mathrm{d}\mathbf{\Omega}_k & \int_{\Omega_k} \varphi_2(\mathbf{x})\varphi_2(\mathbf{x})\mathrm{d}\mathbf{\Omega}_k & \cdots & \int_{\Omega_k} \varphi_2(\mathbf{x})\varphi_n(\mathbf{x})\mathrm{d}\mathbf{\Omega}_k \\ \vdots & \vdots & \ddots & \vdots \\ \int_{\Omega_k} \varphi_n(\mathbf{x})\varphi_1(\mathbf{x})\mathrm{d}\mathbf{\Omega}_k & \int_{\Omega_k} \varphi_n(\mathbf{x})\varphi_2(\mathbf{x})\mathrm{d}\mathbf{\Omega}_k & \cdots & \int_{\Omega_k} \varphi_n(\mathbf{x})\varphi_n(\mathbf{x})\mathrm{d}\mathbf{\Omega}_k \end{bmatrix}, \tag{27}$$

Owing to the orthogonal property of the basis functions, $\mathbf{M} = \begin{cases} C_{ij} & i = j \\ 0 & i \ne j \end{cases}$

$$\mathbf{K} = \int_{\Omega_k} \nabla\varphi_i(\mathbf{x})\varphi_i(\mathbf{x})\mathrm{d}\mathbf{\Omega}_k$$
$$= \begin{bmatrix} \int_{\Omega_k} \nabla\varphi_1(\mathbf{x})\varphi_1(\mathbf{x})\mathrm{d}\mathbf{\Omega}_k & \int_{\Omega_k} \nabla\varphi_1(\mathbf{x})\varphi_2(\mathbf{x})\mathrm{d}\mathbf{\Omega}_k & \cdots & \int_{\Omega_k} \nabla\varphi_1(\mathbf{x})\varphi_n(\mathbf{x})\mathrm{d}\mathbf{\Omega}_k \\ \int_{\Omega_k} \nabla\varphi_2(\mathbf{x})\varphi_1(\mathbf{x})\mathrm{d}\mathbf{\Omega}_k & \int_{\Omega_k} \nabla\varphi_2(\mathbf{x})\varphi_2(\mathbf{x})\mathrm{d}\mathbf{\Omega}_k & \cdots & \int_{\Omega_k} \nabla\varphi_2(\mathbf{x})\varphi_n(\mathbf{x})\mathrm{d}\mathbf{\Omega}_k \\ \vdots & \vdots & \ddots & \vdots \\ \int_{\Omega_k} \nabla\varphi_n(\mathbf{x})\varphi_1(\mathbf{x})\mathrm{d}\mathbf{\Omega}_k & \int_{\Omega_k} \nabla\varphi_n(\mathbf{x})\varphi_2(\mathbf{x})\mathrm{d}\mathbf{\Omega}_k & \cdots & \int_{\Omega_k} \nabla\varphi_n(\mathbf{x})\varphi_n(\mathbf{x})\mathrm{d}\mathbf{\Omega}_k \end{bmatrix} \tag{28}$$

$$\mathbf{\Theta} = \begin{bmatrix} \int_{\Omega_e} \varphi_1(\mathbf{x})\left|J\right|\mathrm{d}\mathbf{\Omega}_e \\ \int_{\Omega_e} \varphi_2(\mathbf{x})\left|J\right|\mathrm{d}\mathbf{\Omega}_e \\ \vdots \\ \int_{\Omega_e} \varphi_n(\mathbf{x})\left|J\right|\mathrm{d}\mathbf{\Omega}_e \end{bmatrix} \tag{29}$$

$$\mathbf{\Theta}' = \begin{bmatrix} \int_{\Omega_e} \varphi_1(\mathbf{x})\left|J'\right|\mathrm{d}\mathbf{\Omega}_e \\ \int_{\Omega_e} \varphi_2(\mathbf{x})\left|J'\right|\mathrm{d}\mathbf{\Omega}_e \\ \vdots \\ \int_{\Omega_e} \varphi_n(\mathbf{x})\left|J'\right|\mathrm{d}\mathbf{\Omega}_e \end{bmatrix}. \tag{30}$$

The choice of orthogonal basis functions greatly simplifies the contribution of the high order moments of the polynomial approximate solution to the source-term related vector $\mathbf{\Theta}'$ in equation (30). Once the basis functions (Legendre polynomials), $\varphi_n(\mathbf{x})$, are multiplied by the transformation Jacobian ($|J'| = (1-b)/2$), the integration in the interval [-1 1] will vanish for all the terms except the first term, due to orthogonal property of the basis functions and a coincidental relation $\varphi_1(\mathbf{x}) = 1$; that is,

$$\mathbf{\Theta}' = \begin{bmatrix} \int_{\Omega_e} \varphi_1(\mathbf{x}) |J'| \mathrm{d}\mathbf{\Omega}_e \\ \int_{\Omega_e} \varphi_2(\mathbf{x}) |J'| \mathrm{d}\mathbf{\Omega}_e \\ \vdots \\ \int_{\Omega_e} \varphi_n(\mathbf{x}) |J'| \mathrm{d}\mathbf{\Omega}_e \end{bmatrix} = \begin{bmatrix} 2 \\ 0 \\ \vdots \\ \vdots \\ 0 \end{bmatrix} \tag{31}$$

Note that, in this novel method, the source term treatment is greatly simplified, exactly the same as the first-order (P^0) case. In other words, the contribution of the cell average solutions is dominant in the source terms in the DG framework, although the left hand side of equations (19) and (25) is calculated by the high order polynomial approximation.

4. Numerical investigation of complex waves in dusty gas flows

In this section, we present the results for some of the well-known benchmark problems in one- and two-dimensional space. For the purpose of verifying the code and estimating the order of accuracy of the numerical scheme, we first solve a smooth problem with analytical solutions. We then investigate the widely studied Sod's shock tube problem in dusty gas flows with special emphasis on the complex wave behaviors therein. Finally, we solve two two-dimensional multiphase flows—explosion and compression corner problems—to highlight the effects of the dispersed phase (solid dust) on multi-dimensional dusty gas flow. In all test cases, the ratio of the specific heats of air (γ) and the ratio of the specific heats of the two phases (c_m/c_v) are set equal to 1.4 and 1.0, respectively. Unless otherwise mentioned, the following values are used for particle properties:

diameter, d=10 μm;

mass density, ρ_s=2,500 kg/m^3;

specific heat, c_m=718 J/kg-K.

4.1. Verification study in the single-phase case

The propagation of a smooth sine wave was considered for verification of the code. The periodic boundary conditions were applied at both sides of the domain. For the following initial condition,

$$\begin{cases} u(x,0)=1, \\ \rho(x,0)=1.0+0.2\sin(\pi x), \\ p(x,0)=1, \end{cases} \tag{32}$$

the corresponding exact solutions can be written as

$$\begin{cases} u(x,t)=1, \\ \rho(x,t)=1.0+0.2\sin(\pi(x-t)), \\ p(x,t)=1. \end{cases} \tag{33}$$

In order to measure the order of accuracy of the DG method for various flux functions, the density distribution of the solution was obtained for different orders of accuracy (P^χ, with χ indicating the polynomial order) and the results are shown in Fig. 4. It can be seen that numerical deviation from the analytical solution is large in the first-order piecewise constant case (P^0); however, the application of more sophisticated numerical fluxes such as Roe and HLL can improve the accuracy of the piecewise constant solution.

In order to evaluate the performance of the numerical scheme in more detail, the numerical errors and the order of accuracy were calculated based on the density solution. The

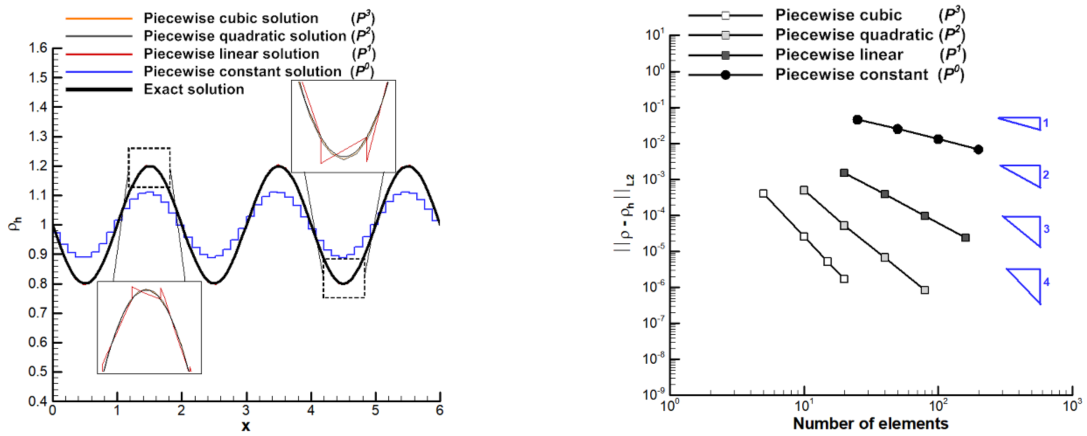

Roe flux function

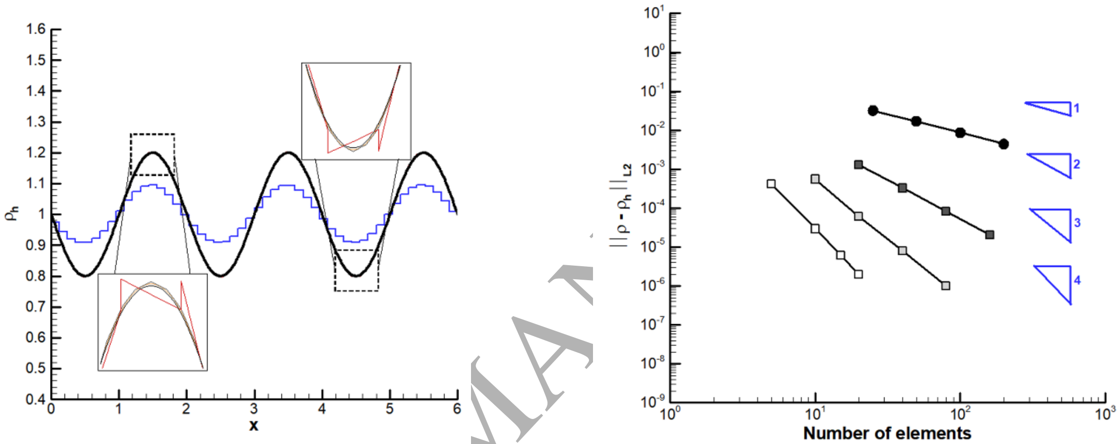

HLL flux function

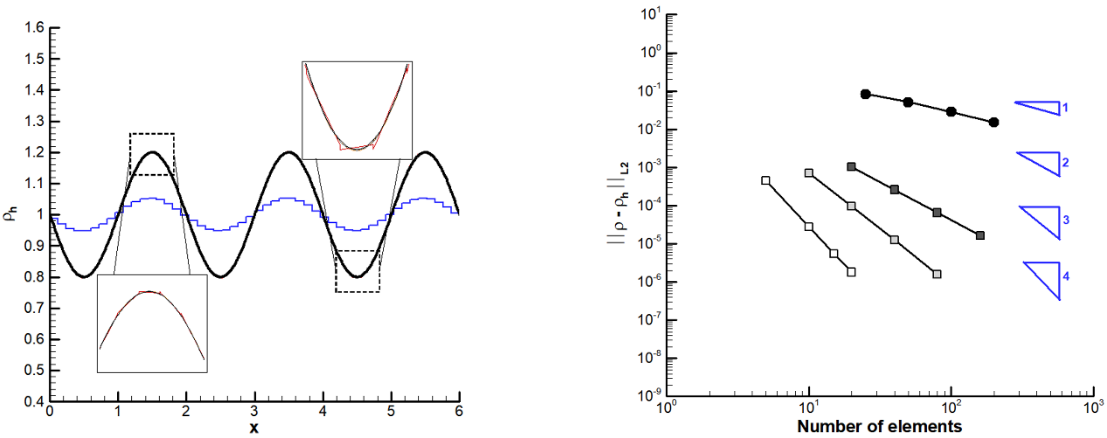

Rusanov (LLF) flux function

Fig. 4. Comparison of various numerical fluxes for smooth solution of Euler equation; (left) profile, (right) Euclidean norm of density

results were found to be consistent with the observations of Qiu et al. (2006). Moreover, it was confirmed that all numerical fluxes lead to the expected order of accuracy of P+1. It is worth noting that each flux function shows a different behavior in performance for different orders of polynomial function, and thus drawing a general conclusion is not possible.

4.2. Sod shock tube problem in dusty gas flows

Fig. 5 depicts the shock tube problem in single phase (pure gas) and multiphase (dusty gas). The evolution of various types of waves and discontinuities from the initial Riemann data can provide the essence of dusty gas flows; as, for example, the supersonic flows formed by the interaction of rocket plume and lunar dust. Moreover, the shock tube problem is ideal for examining the feasibility and validity of the new numerical methods, since it is free from boundary effects or other numerical complexities. The scheme tested in the one dimension problem can also be extended to the multi-dimensional situation afterwards.

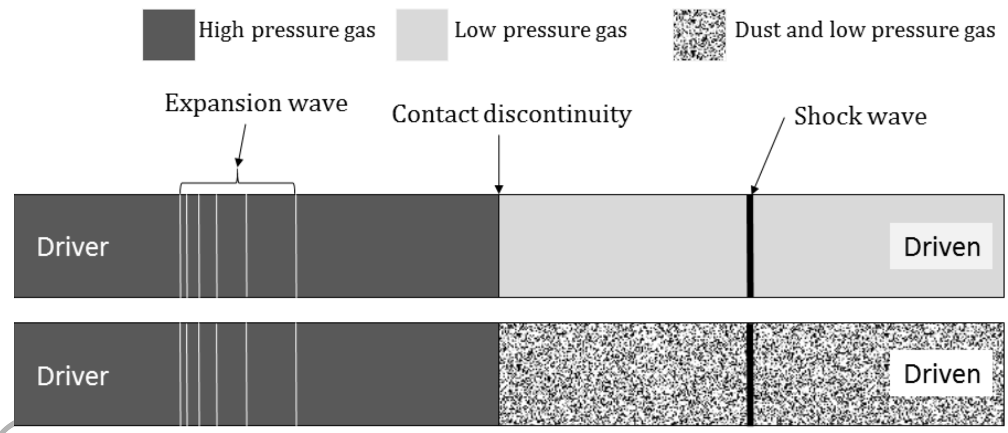

Fig. 5. Schematic of the shock tube problem in dusty gas (pure gas versus dusty gas) (computational domain length: $100L$)

In order to obtain solutions without spurious oscillations, the positivity-preserving scheme was used in conjunction with the monotonicity-preserving limiter. It should be emphasized again that no extra effort is necessary for handling the source terms, thanks to the special feature associated with the orthogonal basis functions introduced in the new DG scheme, as explained in subsection 3.5. That is, the present DG method is immune to the artifact that may arise from splitting the source terms, or the complexity incurred by application of the fractional step approach (Gurris et al., 2010; Perot, 1993) or the random choice method (Saito and Glass, 1984) to cope with the source terms.

The results of the dusty shock tube problem with the initial condition summarized in Table 1 are presented in Fig. 6. It can be seen that the numerical solutions of the pure gas are in good agreement with the analytical solutions of the shock tube problem. In the figures, the term 'dusy gas' implies the carrier gas phase. This problem has been previously investigated by Saito (2002), Saito et al. (2003) and Pelanti and LeVeque (2006). Comparison with these previous results can be used as verification of the present computational model of two-fluid dusty gas. The multiphase solutions clearly demonstrate the profound effects of the inertia of the dust particles on the flow properties. The gradual response of the dust particles to the diaphragm rupture was observed, especially in the velocity and temperature profiles. Interestingly, the strength of the right-running shock wave front was found to be much smaller than that of pure gas, which is due to the absorption of momentum and heat from the gas molecules by the dust particles. In addition, the deceleration of the shock wave front was observed from the velocity profile, inducing compression waves behind the shock wave. This phenomenon was identified in the pressure profiles as well.

Table 1. Initial condition for the Sod's shock tube problem

Non-dimensional variable	Driver section	Driven section
Pressure	10.0	1.0
Gas density	10.0	1.0
Particle concentration	0.00001	1.0
Gas velocity	0.0	0.0
Dust velocity	0.0	0.0

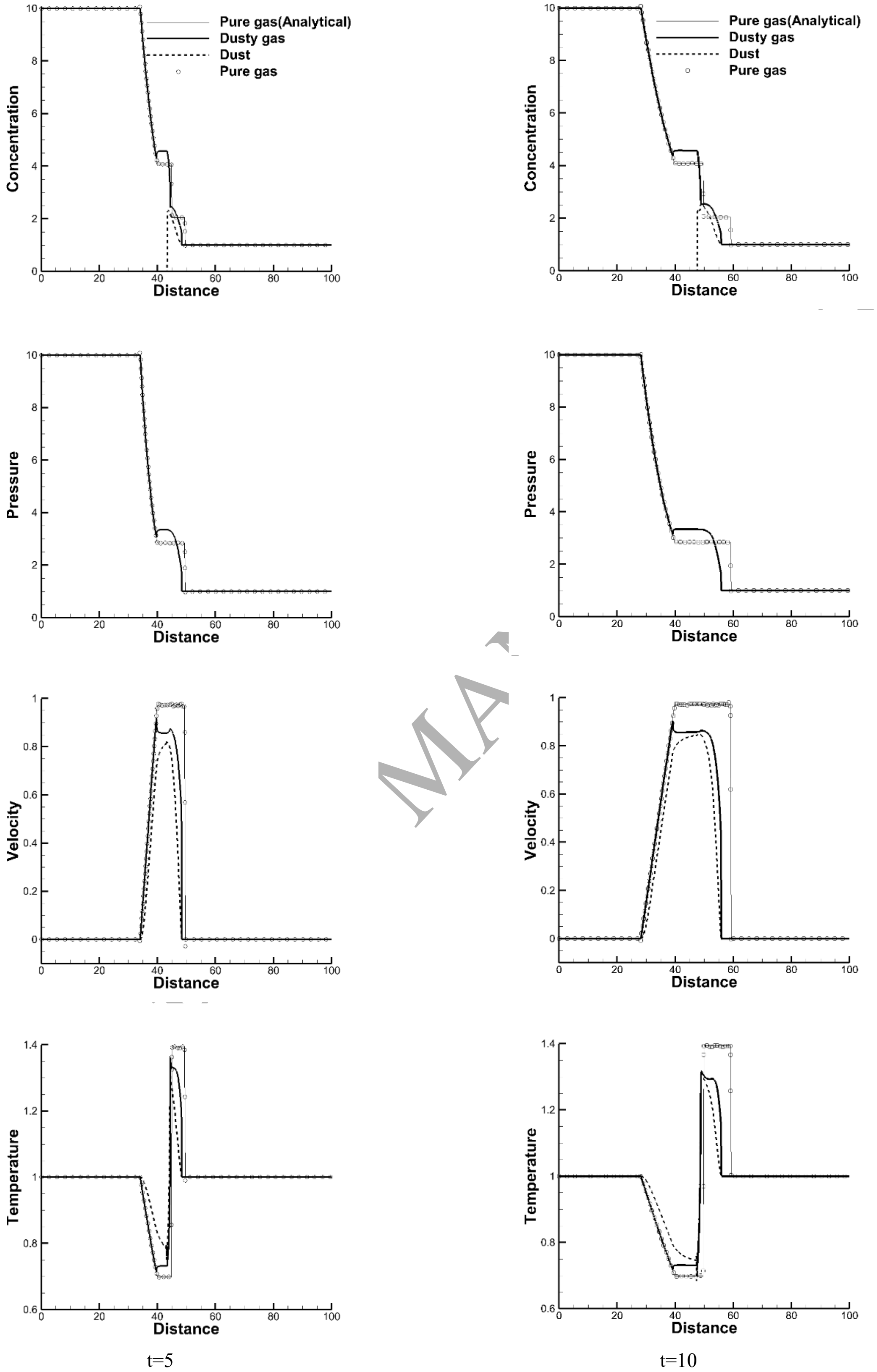

Fig. 6. Solutions of the Sod's shock tube problem in dusty gas for two different time steps (P^1 solution)

4.3. Composite wave structures in the Sod problem of dusty gas flows

In contrast to a single-phase flow, dusty gas flows can show some striking wave structures, which have no counterpart in classical theory. The physical explanation of these phenomena in dusty gas flows has rarely been addressed in the literatures. In this section, we provide a detailed discussion on the underlying physics forming these abnormal waves.

Various wave structures that are formed in the shock tube problem of dusty gases are schematically illustrated using the *x*-*t* diagram in Fig. 7 (a) describes the case in which the contact discontinuity of gas and the boundary path of a particle are located at the same position, while Fig. 7 (b) describes the case in which the boundary path of a particle is located at a distance from the contact discontinuity of gas. When a shock wave impinges on a cloud of particles in dusty gas flows, it will be reflected as an expansion or shock wave, depending on the ratio of the specific heats of the solid particle and gas, and the particulate loading of the mixture (Sommerfeld, 1985). In this diagram, the case of reflected rarefaction waves was not considered, since the properties of the test case of the mixture correspond to the case of shock wave reflection. Since solid particles with non-negligible inertia cannot follow the abrupt changes of flow, a relaxation zone attached to the shock wave forms and the shock wave front decelerates until a new equilibrium condition is reached. The size of the relaxation zone is affected by the diameter of the solid particle, density, and heat capacity. As mentioned before, a finite time is required for the particles to fully attain the speed of the gas. During this period, reflected compression waves are generated from the boundary path of the particle, eventually forming a weak left-running shock wave, as illustrated in Fig. 7 (a).

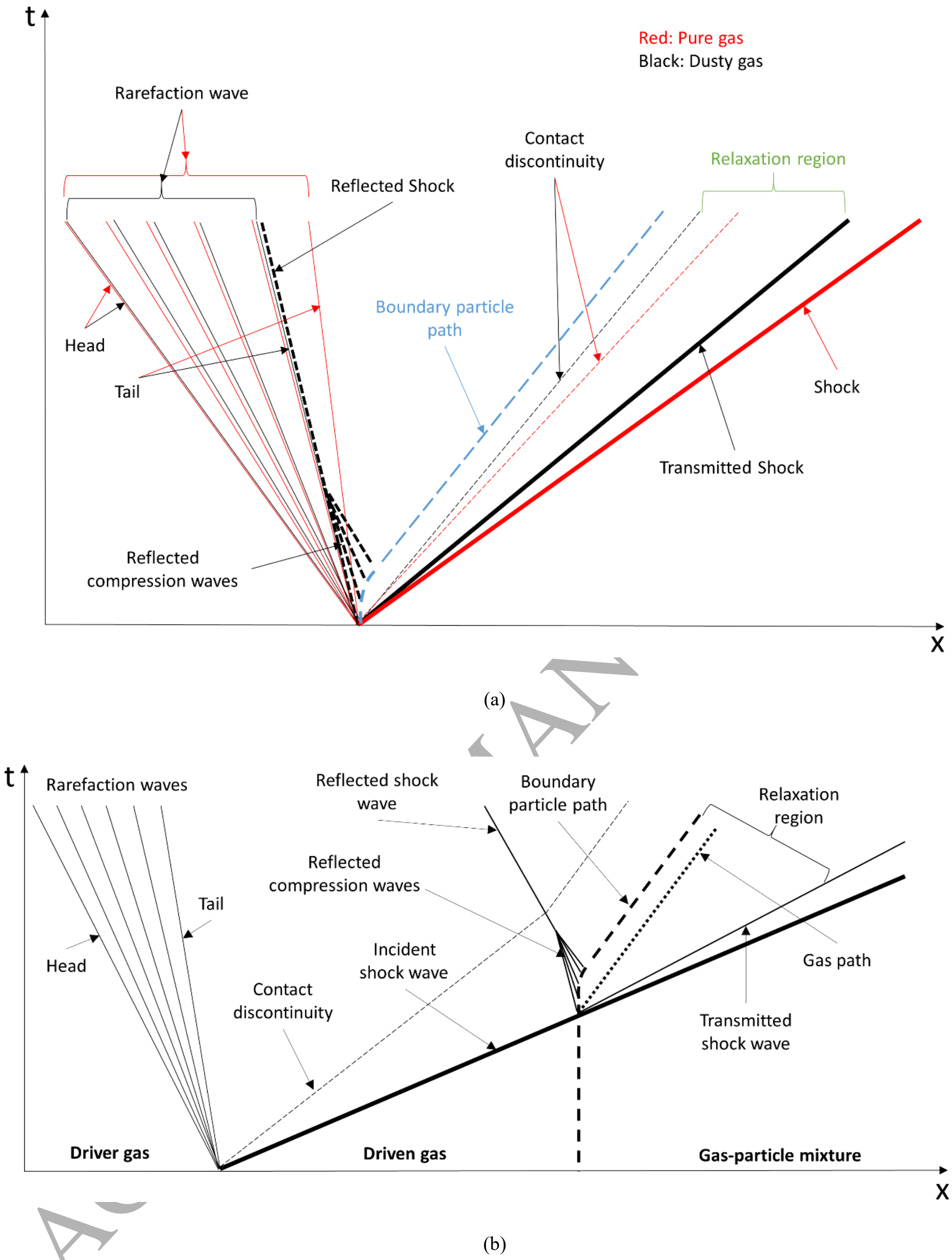

Fig. 7. Schematic of various wave structures in the 1-D dusty gas flows: (a) The gas contact discontinuity and boundary particle path are initially located at the same position, (b) The particle boundary path is located at a distance from the gas phase contact discontinuity.

The effects of particle concentration are shown in Fig. 8, with a focus on abnormal behaviors. The non-dimensional time of 30 was chosen so that the flow becomes fully developed, enabling a better description of the phenomena. It can be clearly observed that a higher concentration of dust particles in the driven section of the shock tube leads to amplification of the effects (at the tale of the left-running rarefaction waves and the right-running shock wave, and pre-contact discontinuity). Therefore, one may conclude that the presence of dust particles is the main source of these behaviors.

For better clarification, we investigated in detail how the evolution of those waves is affected by the concentration of dust particles. We identified three abnormal behaviors based on the density profile: 1) the tale of the left-running rarefaction waves; 2) the region before the contact discontinuity; and 3) the tale of the right-running shock wave. It is well known that, after the diaphragm ruptures, a right-running compression wave and left-running rarefaction waves will start to propagate in the background medium. On the other hand, dust particles with different density ratios on each side of the diaphragm will lead to the existence of an extra contact discontinuity (in solid phase) compared to the case of pure gas. We refer to this discontinuity as the dust contact discontinuity (DCD).

The first composite wave structure, marked as number (1) in Fig. 8, was observed at the tail of the rarefaction waves in the density profile. This exotic structure should be distinguished from the numerical artifacts that may be found in high order methods when they are not treated properly. Due to the presence of dust particles, the rarefaction waves weaken and their propagation speed decreases as well. Therefore, gas will accumulate in the region close to the tail of the rarefaction waves, and the reflected compression waves generated from the boundary path of the dust particle will form a weak shock wave attached to the tail of the left-running rarefaction waves, as observed in Fig. 8 (a).

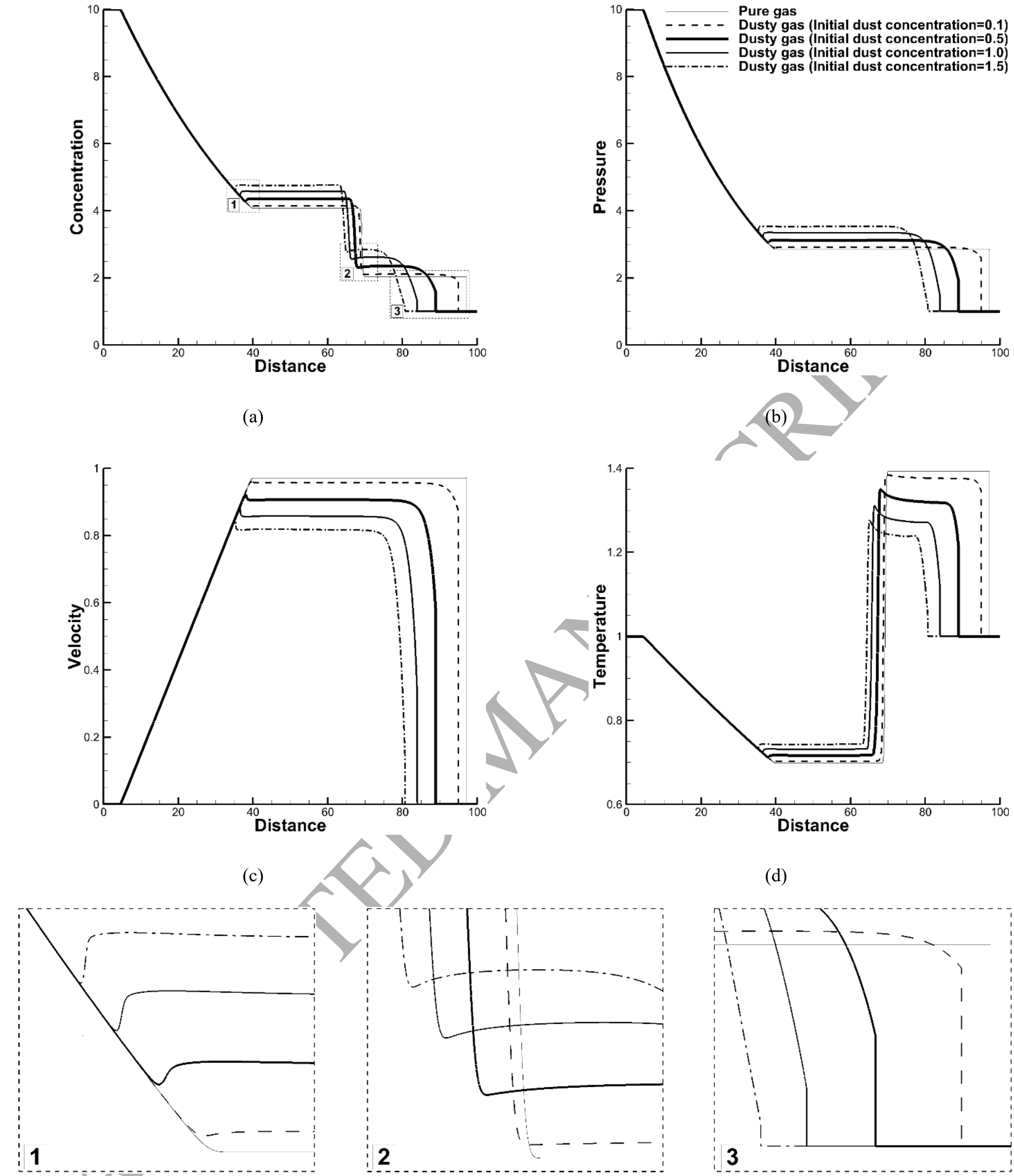

Pseudo compound wave made up of RW-RS

CD attached to RZ

RZ attached to SW

Fig. 8. Effects of initial dust concentration on the Sod's shock tube in the dusty gas (P^1 solution)

(RW: rarefaction wave, RS: reflected shock, CD: contact discontinuity, RZ: relaxation zone, SW: shock wave)

This weak shock wave is directly related to the presence of the DCD and it will be strengthened when the dust concentration increases. It will be shown in a later figure that, when there is no DCD, i.e., when both the high and low pressure sections are filled with the same dust concentration, this composite wave structure will disappear. In passing, it should be mentioned that this type of composite waves is different from the generic compound waves observed in magneto-hydrodynamics, due to the non-convexity and the non-strict hyperbolicity (Myong and Roe, 1997), and the present waves should be called composite waves or pseudo-compound waves, rather than compound waves.

In another region, marked number (2) in Fig. 8, the presence of dust induces an increase in pressure (and a decrease in velocity) in the middle region, leading to higher density compared to the case of. It turns out that this increase in density is dependent on dust concentration, as well as the location of the DCD.

A second composite wave structure, marked number (3) in Fig. 8, was observed at the tail of the shock wave. It consists of a right-running shock wave followed by a relaxation zone. When there is no particle, the shock wave is steep and strong as expected. When particles are present, however, the shock wave weakens substantially and the relaxation zone forms instead, due to the coupling effects between the two phases. We can clearly see that a higher particle concentration leads to a larger relaxation zone and a reduction in the propagation speed of the shock wave. It will be shown in the next figure that the location of the DCD changes the position where the shock wave forms, but does not affect the size of the relaxation zone.

In order to investigate how the DCD would affect wave patterns in the dusty gas flows, additional cases were simulated by varying the position of the DCD (from x=40 to x=60) while maintaining the same dust concentration, as shown in Fig. 9. The other profiles in this

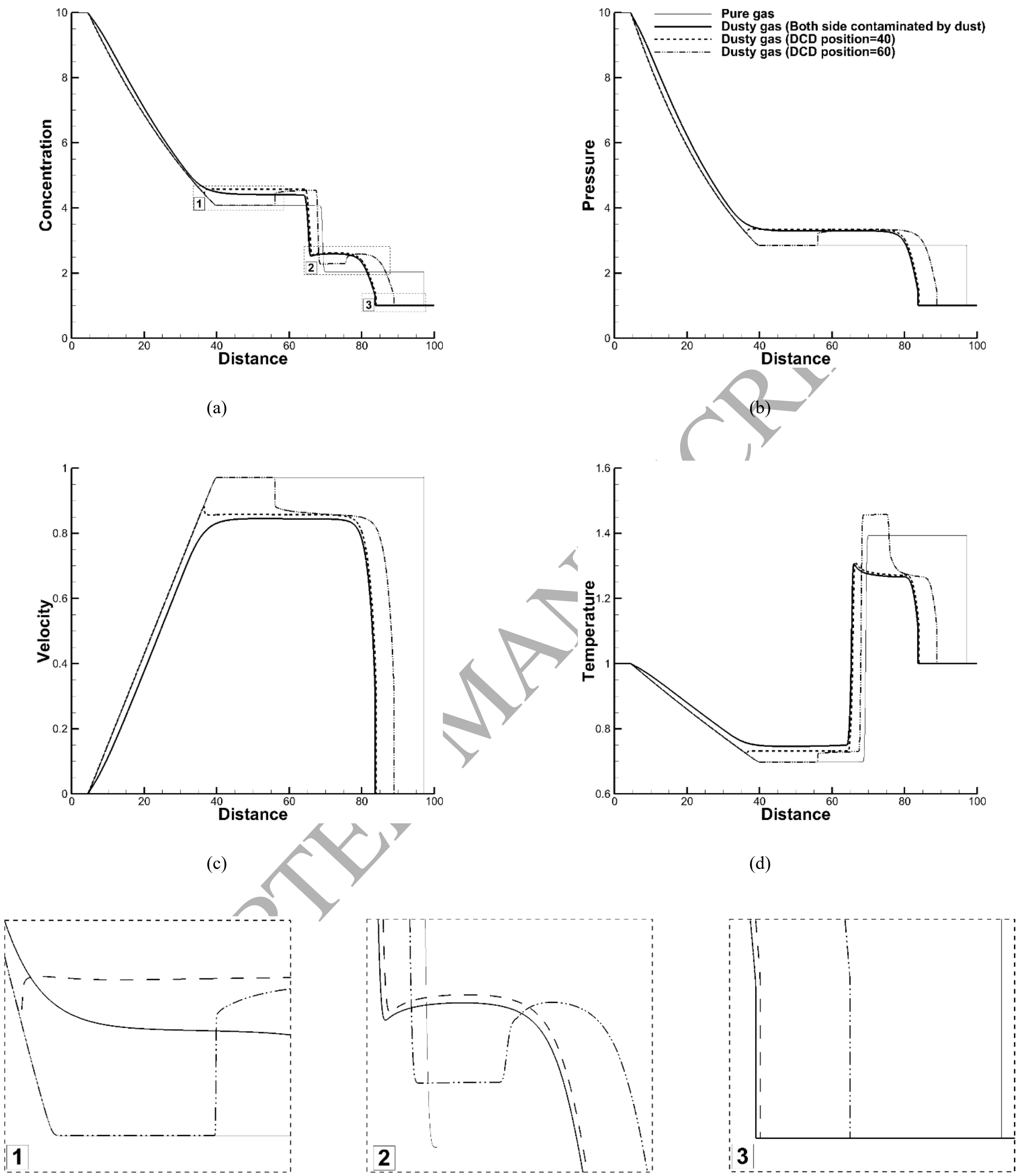

Pseudo compound wave made up of RW-RS

CD attached/detached to/from RZ

RZ attached to SW

Fig. 9. Effects of location of the initial dust contact discontinuity (DCD) on the Sod's shock tube in the dusty gas at t=30 (P^1 solution) (RW: rarefaction wave, RS: reflected shock, CD: contact discontinuity, RZ: relaxation zone, SW: shock wave)

figure correspond to the pure gas and the dusty gas case of the previous figure. In all cases, the dust concentration is assigned with the same value ($\alpha_0\rho_0$=0.1). In the region marked number (1), the weak discontinuity in density, pressure and temperature profiles discussed in Fig. 8 vanishes when there is no DCD. When the DCD is shifted towards the right end of the tube (x=60), the discontinuity is detached from the rarefaction waves and is shifted to the right as well.

In the region marked number (2), the shifted DCD seems to produce yet another contact discontinuity (around x=70) attached to the relaxation zone. When put together with adjacent waves, there seems to be a new composite wave structure, consisting of three waves—a contact discontinuity, the relaxation zone, and a shock wave. On the other hand, as can be seen in region number (3), the strength of the right-running shock wave and the size of the relaxation zone remain the same for all dusty gas cases, though the position of the waves is shifted as expected.

4.4. 2-D explosion problem in dusty gas flows

As the first two-dimensional test case, we investigated the explosion problem outlined in Toro (2013) for a pure gas. This problem is in essence the two-dimensional extension of the classical Sod's shock tube, as illustrated in Fig. 10.

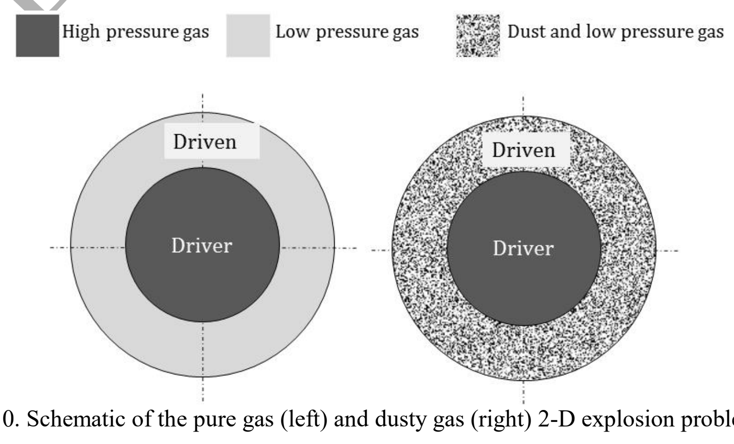

Fig. 10. Schematic of the pure gas (left) and dusty gas (right) 2-D explosion problems (outer radius: L)

The initial conditions for the single-phase and multiphase cases are summarized in Table 2.

Table 2. Initial condition for the explosion problem

Non-dimensional variable	Driver section	Driven section
Pressure	1.0	0.1
Gas density	1.0	0.125
Particle concentration	0.00001	0.1
Gas velocity	0.0	0.0
Dust velocity	0.0	0.0

A study on grid independency is presented in Fig. 11 where five different grids with mesh sizes of h=1/20, 1/40, 1/80, 1/120 and 1/160 are considered, where h is the characteristic size of grid. A grid resolution with h=1/120 was found to provide almost identical results with h=1/160, and hence this grid was used for the rest of simulations.

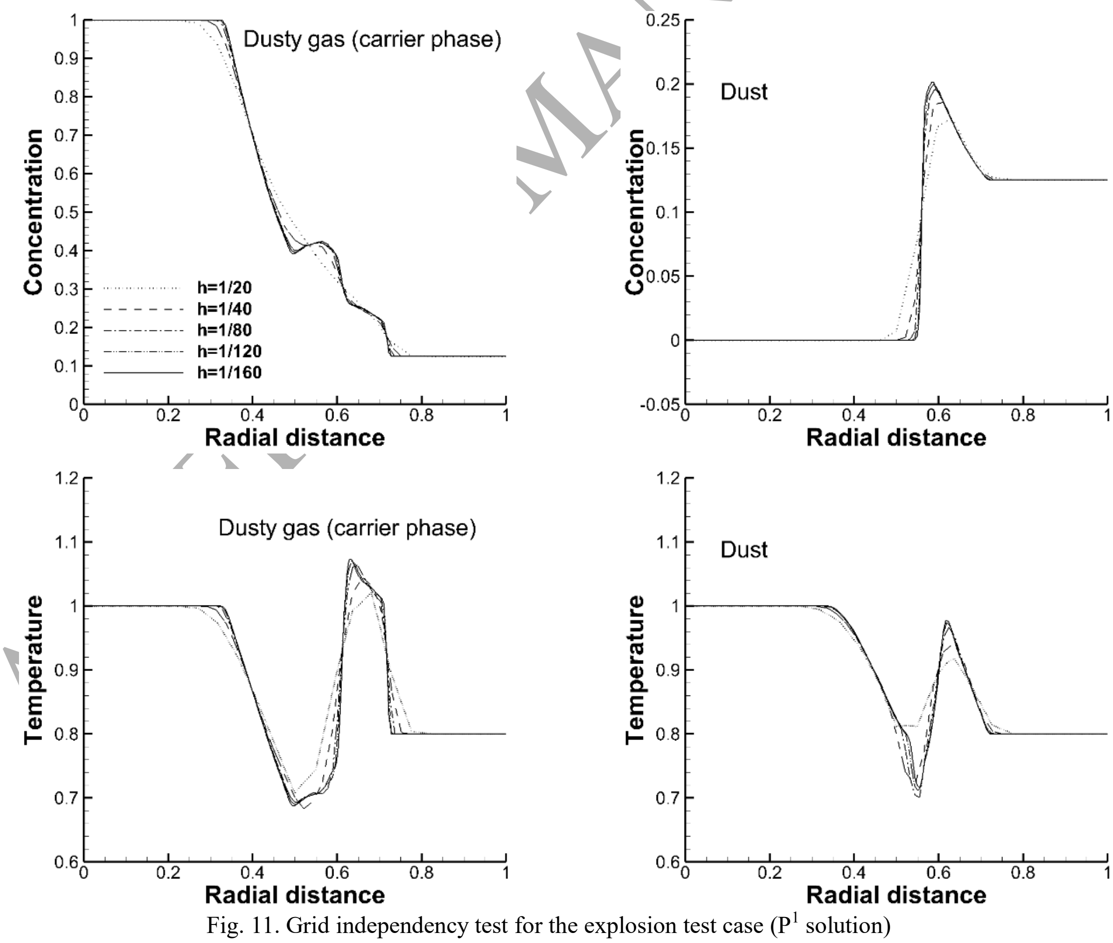

Fig. 11. Grid independency test for the explosion test case (P^1 solution)

In the next step, the effects of the polynomial order of the DG method was examined with and without the monotonicity preserving limiter for the single-phase problem, while the positivity preserving limiter was applied for all cases. It can be seen in the left column of Fig. 12 that, without the monotonicity preserving limiter, the second- and third-order solutions exhibit severe oscillations near strong waves. The Barth-Jespersen limiter described in subsection 3.3, however, was shown to handle the non-physical oscillations effectively, as confirmed in the right column of Fig. 12. Our numerical experiments showed that such oscillations lead to a breakdown of the numerical code, in the case of high CFL numbers, or when multiphase problems are solved without proper monotonicity preserving limiters. The judicious use of limiters specially developed for the DG method, along with the discontinuity detection scheme, is believed to be key factors in the successful shock capture with a minimum penalty in accuracy.

In addition, we investigated the evolution of the gas and solid phase concentrations, as summarized in Fig. 13 and Fig. 14. The initial conditions for this multiphase case are given in Table 2. The physical justifications obtained from the one-dimensional Sod's shock tube in dusty gas flows hold true here. That is, the presence of dust particles leads to a weakened shock wave whose front is cut by the relaxation zone. Moreover, for the same reason, the shock wave front decelerates substantially as time elapses.

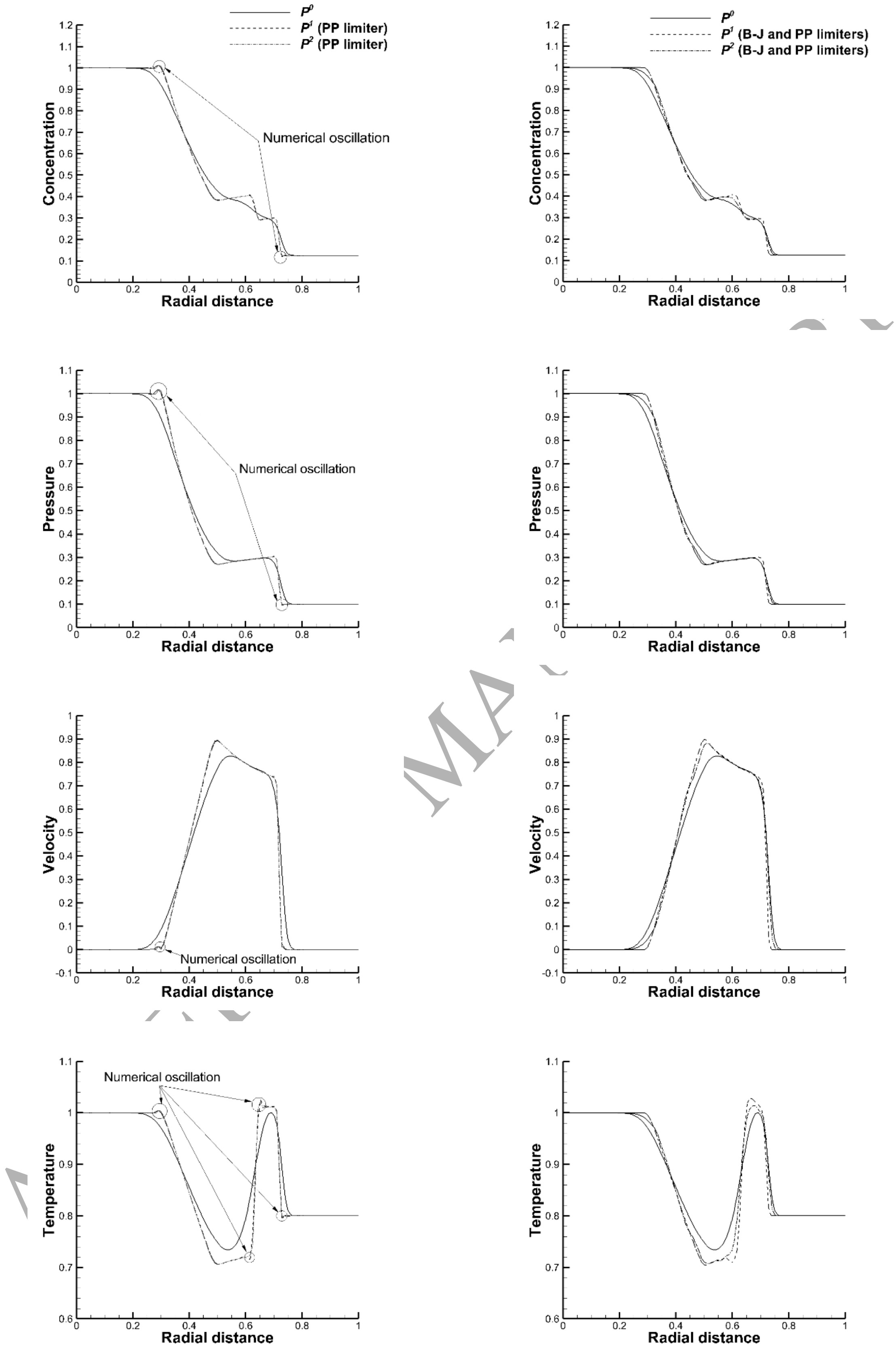

Fig. 12. High order solutions of the explosion problem for pure gas (h=1/100, t=0.2)

Without monotonicity preserving limiter (left); with monotonicity preserving limiter (right) (P^1 solution)

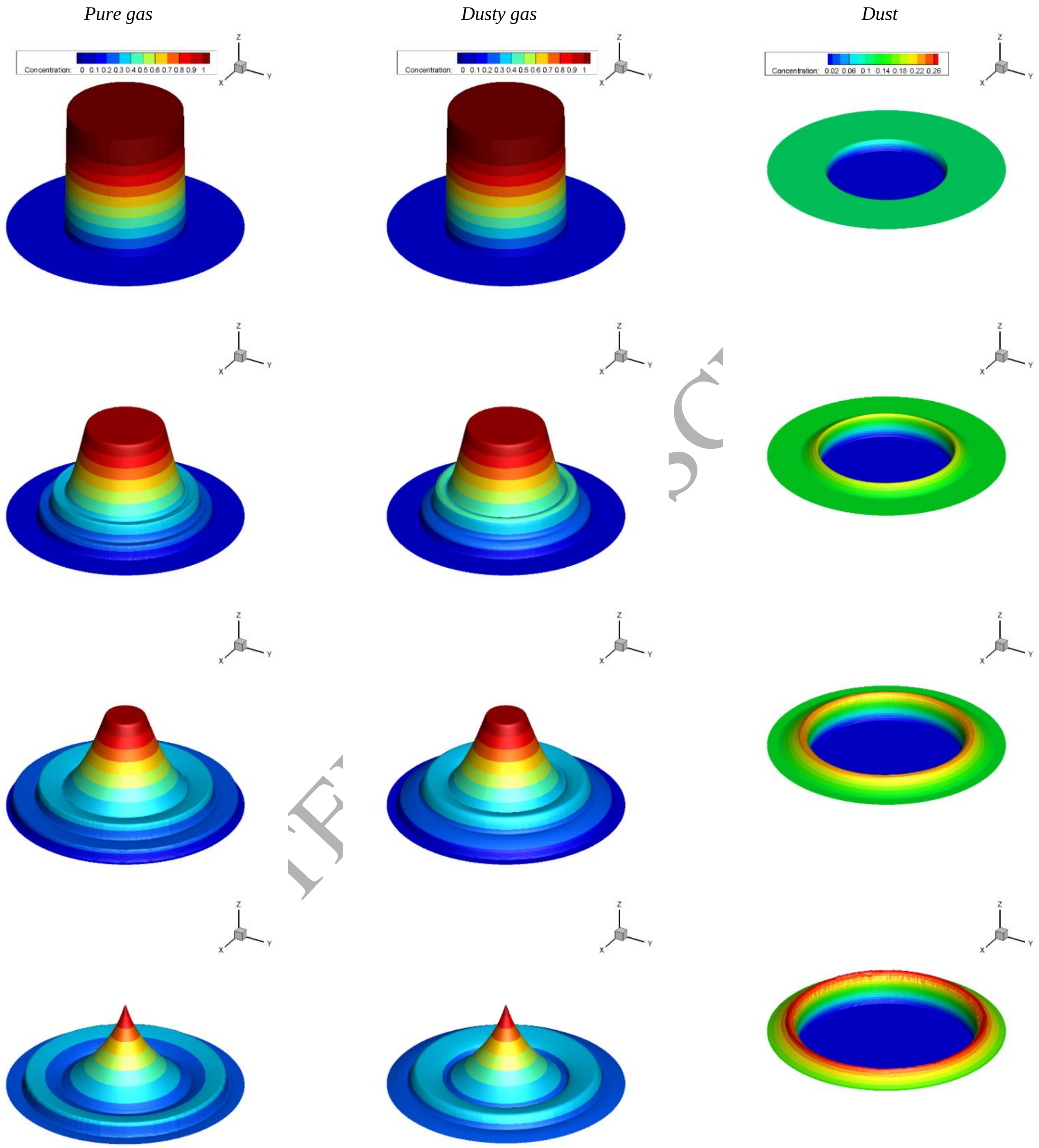

Fig. 13. Graphical presentation of time evolution of density in the multiphase explosion problem (P^1 solution)

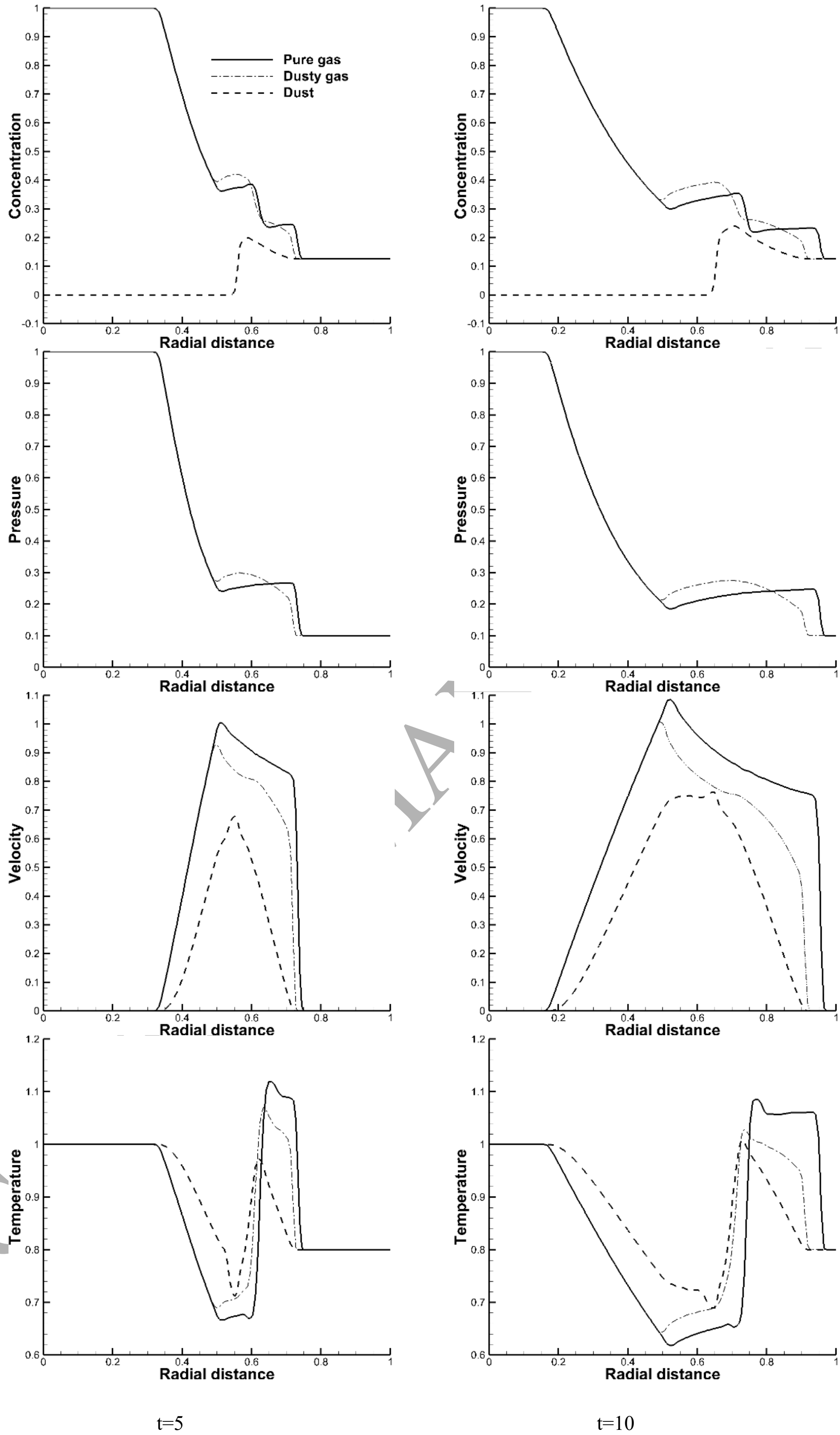

Fig. 14. Time evolution in the multiphase explosion problem (P^1 solution)

4.5. 2-D compression corner problem in dusty gas flow

As the second two-dimensional benchmark problem, we investigated the compression corner problem for both the single and multi-phase applications. This problem is far more complicated due to the presences of boundary effects and the intrinsic complexity of the flow. The incident shock Mach number M_s, the wall inclination angel θ_w, and the initial condition of driven and driver sections define the governing physics of the shock-wave diffraction. The schematic of the compression corner problem is illustrated in Fig. 15.

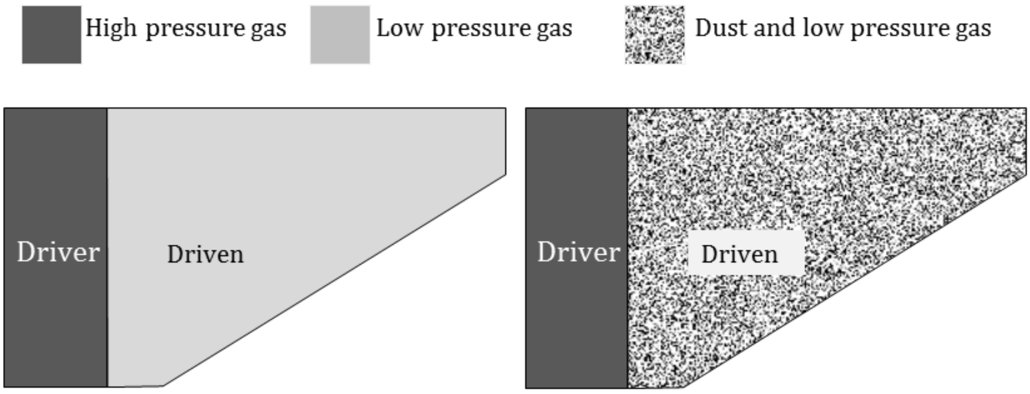

Fig. 15. Schematic of the pure gas (left) and dusty gas (right) 2-D compression corner problems (computational domain size: $5L\times4L$)

As a validation study, we compared our numerical solutions with the experimental results obtained by (Deschambault and Glass, 1983) for the case of a single Mach reflection (SMR). The initial condition are for both the single-phase and multiphase cases are provide in

Table 3. Initial condition for the single Mach reflection problem

Non-dimensional variable	Driver section	Driven section
Pressure	4.64	1.0
Gas density	2.71	1.4
Particle concentration	0.1	0.1
Gas velocity (x-direction)	1.51	0.0
Gas velocity (y-direction)	0.0	0.0
Dust velocity (x and y -directions)	0.0	0.0

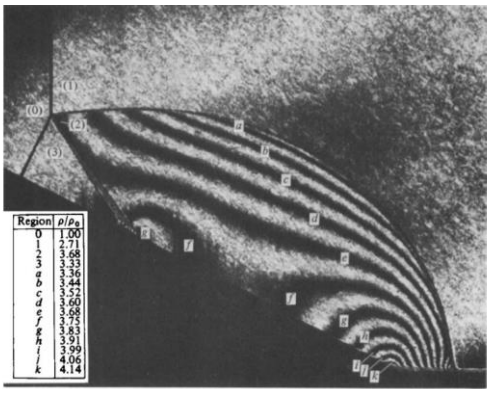

Experimental image (Deschambault and Glass, 1983)

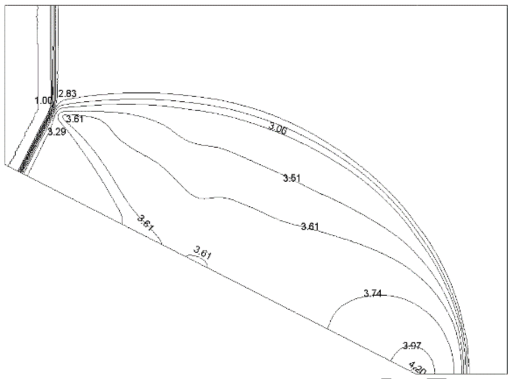

P^0 soloution

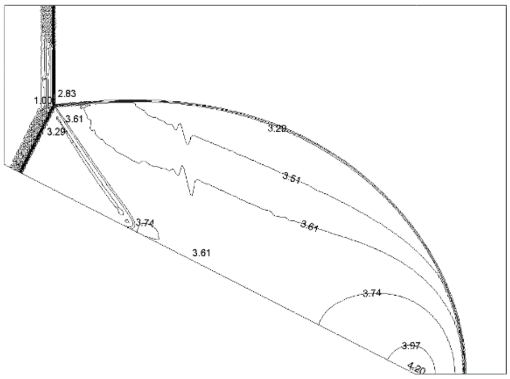

P^1 soloution

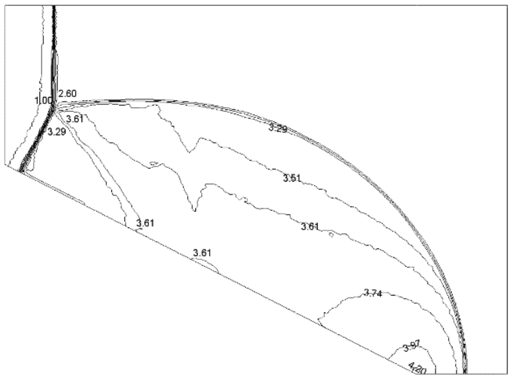

P^2 soloution

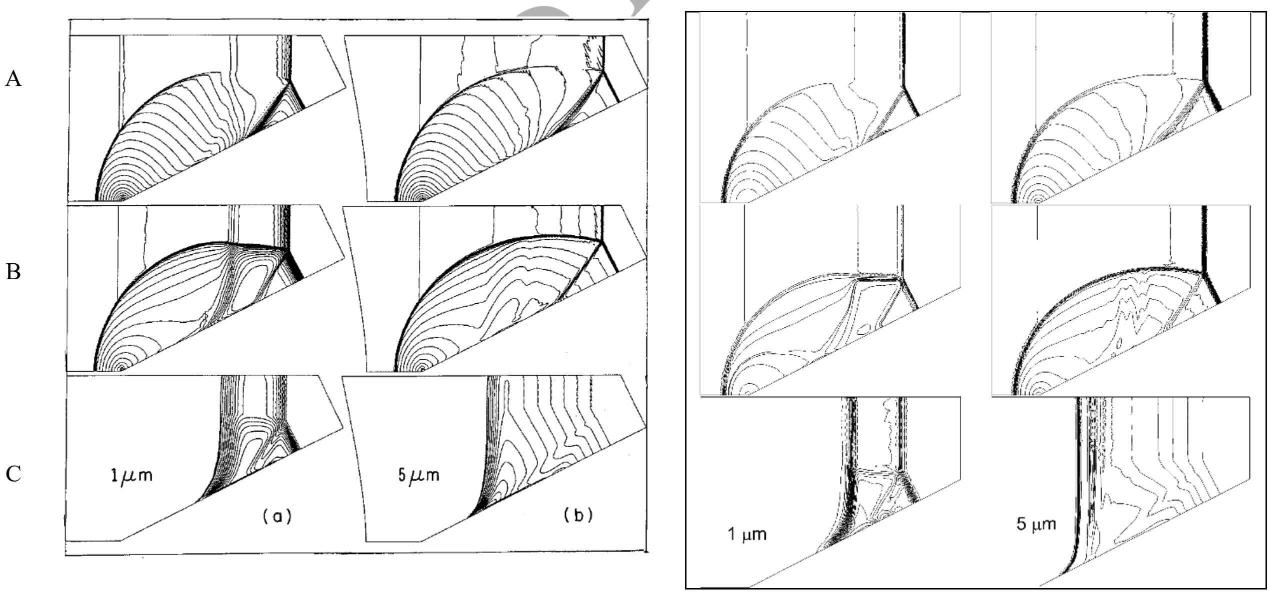

Ben-Dor et al. (2001) Present result (P^1 solution)

Fig. 16. Validation of pure gas case (Isopycnics for single Mach reflection: M_s=*2.03* and θ_w=*27°*) and verification of dusty gas case (A-constant flow Mach number contours, B-constant gaseous phase density contours, and C-constant dust phase spatial density)

table 3. The incident shock Mach number is set to 2.03, and the corner wedge angel is given by 27°. Numerical solutions, up to the third order of accuracy, were in good agreement with experimental data, as shown in Fig. 16. We confine our validation to a single-phase SMR case, since no experimental data are available in the case of dusty gas flows. The comparison shows that the solutions up to third order accuracy (P^2) are in good agreement with the experimental data. Also, we verified the dusty gas results with the solutions of (Ben-Dor et al., 2001) for two particle diameters (1 μm and 5μm) in the case of SMR. The comparison of Mach contours as well as isopycnic surfaces of gas and dust densities indicates a good agreement.

Furthermore, a very strong shock wave case studied by Woodward and Colella (1984) was investigated. The problem, a strong Mach 10 shock impinging on a wall inclined at 30°, was known to lead to a complicated double Mach reflection (DMR). The initial conditions for both the single-phase and multiphase cases are summarized in Table 4.

Table 4. Initial condition for the double Mach reflection problem

Non-dimensional variable	Driver section	Driven section
Pressure	116.5	1.0
Gas density	8.0	1.4
Particle concentration	0.1	0.1
Gas velocity (x-direction)	8.25	0.0
Gas velocity (y-direction)	0.0	0.0
Dust velocity (x and y -directions)	0.0	0.0

In Fig. 17 (a), a study on grid independency was done for solutions with the second order of accuracy (P^1). A grid resolution with h=1/100 was found to provide almost identical results with h=1/120, and hence the grid with h=1/100 was used throughout. The density and Mach contours at non-dimensional time t=200, as shown in Fig. 17 (b) and (c), indicated that the present DG scheme successfully resolves all the important flow features: slip lines, Mach stem, secondary Mach stem, reflected shock wave, and the formation of supersonic flow in the delta region. A weak jetting effect reported in Ben-Dor et al. (2001) was also observed.

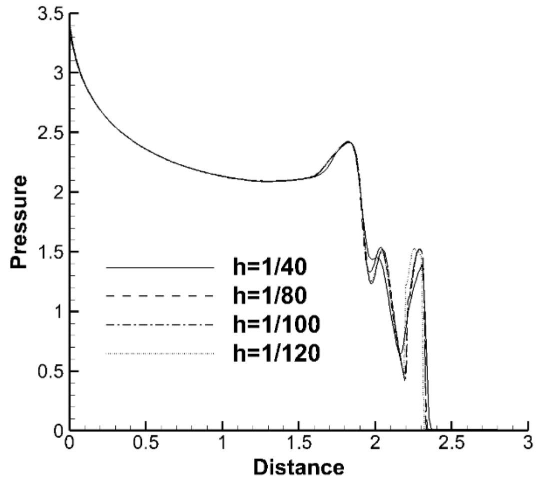

(a) Grid independency study: Pressure distribution along the reflecting wedge surface

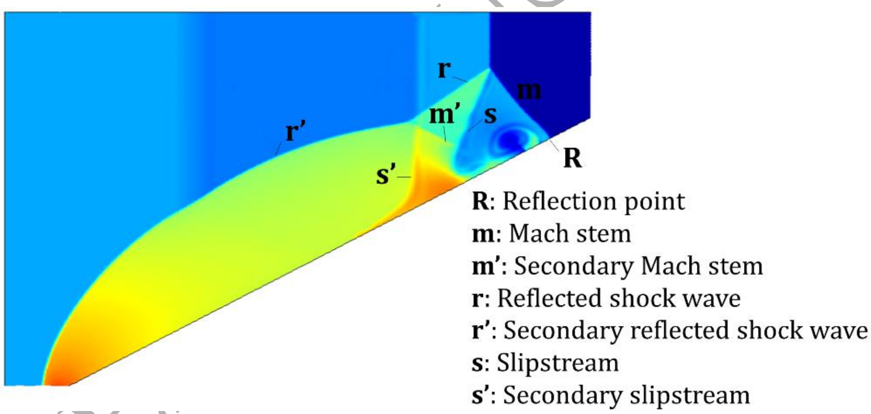

(b) Density contour

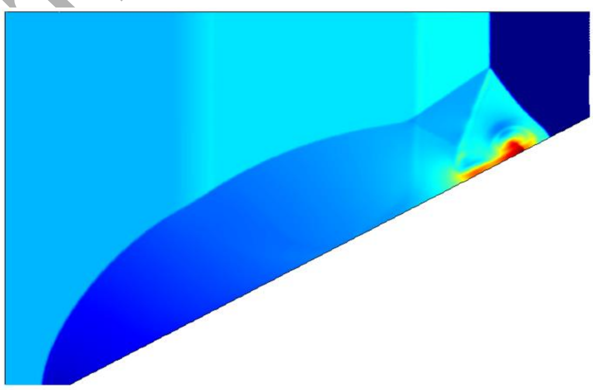

(c) Mach contour

Fig. 17. Verification study: Double Mach reflection (pure gas P^1 solution)

The effects of polynomial order on numerical solutions were analyzed in Fig. 18. It can be clearly seen that the first-order solution with h=1/100 cannot resolve the expected flow feature properly. However, higher order solutions can provide a satisfactory resolution to accurately explain the important physical features of the flow. It can also be seen that there is no drastic change in solutions when increasing the polynomial order from one (P^1) to two (P^2). It should be mentioned that application of the positivity preserving scheme is necessary to prevent numerical instabilities in this high Mach number flow.

In order to understand the effects of dust particles on the time evolution of the flow, the single-phase and multiphase solutions (pure gas, dusty gas, and dust concentration) are summarized in Fig. 19 for two different time steps. One of the main features of the dusty gas flows is that the transition region in the shock waves is much thicker than that of the pure gas. In the multiphase flow, as the shock front is decelerated due to interaction with particles, a longer time is required for the shock front to reach the same location when there is no particle in the flow field. It is also obvious that the presence of the particles can lead to attenuation of the incident shock wave. It should be mentioned that both the positivity and monotonicity preserving limiters were applied in the simulation of multiphase flows to prevent the numerical breakdown.

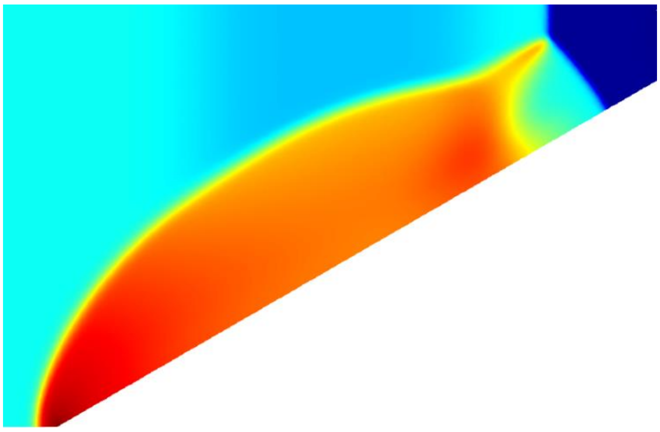

(a) Pure gas (P^0)

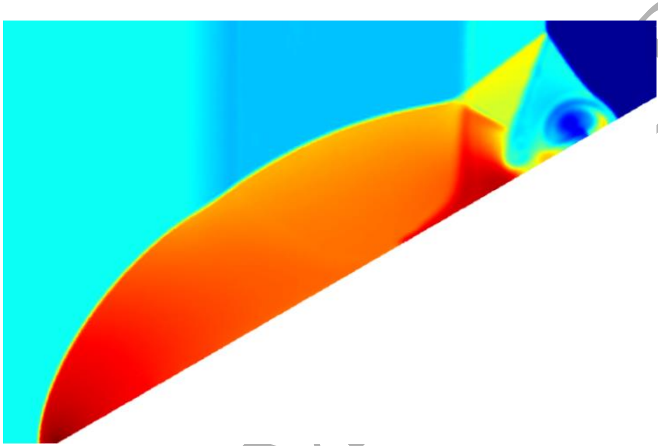

(b) Pure gas (P^1)

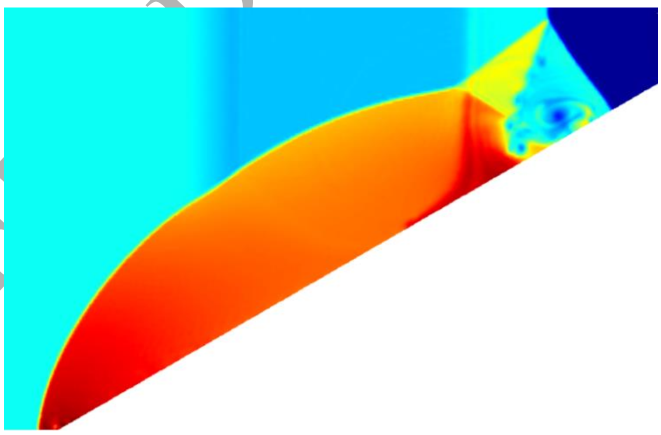

(c) Pure gas (P^2)

Fig. 18. Effects of polynomial orders on the density contours

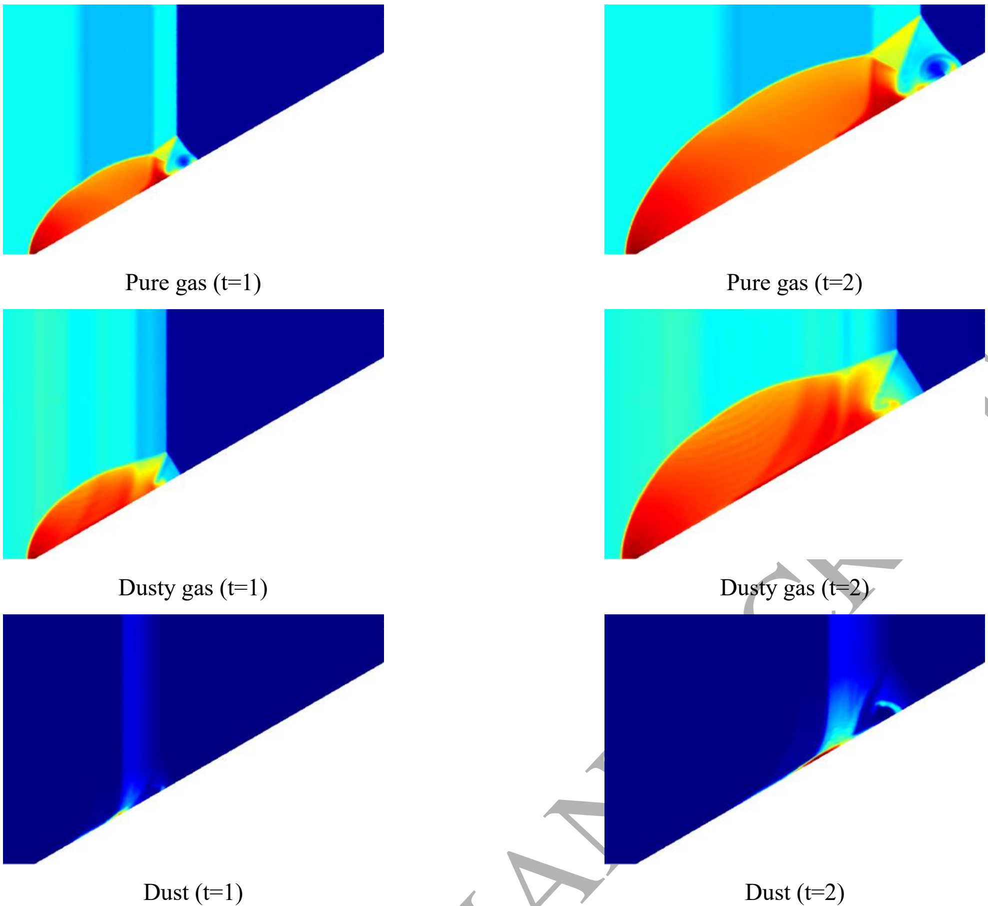

Fig. 19. Time evolution of density contours in the compression corner (double Mach reflection) problem (P^1 solution)

The effects of dust particles on the structure of the DMR were also investigated, as summarized in Fig. 20. The convex shape of the Mach stem in the pure gas simulation is due to the front of the curled slipstream reaching the Mach stem (Li and Ben-Dor, 1999). The presence of particles, however, decelerates the velocity of the slipstream front and does not allow the slipstream to catch up with the Mach stem, as shown in Fig. 20 (b) of the multiphase case with a particulate loading β=0.1 and a particle diameter 10 μm. As a result, the Mach stem forms almost perpendicular to the reflecting wall surface in the dusty gas case. The secondary reflected shock wave and slipstream are severely distorted so that they are not clearly identified. Moreover, the secondary triple point configuration, in which the secondary reflected shock wave, Mach stem and slipstream coincide undergoes a significant change so that such a point is almost indistinguishable.

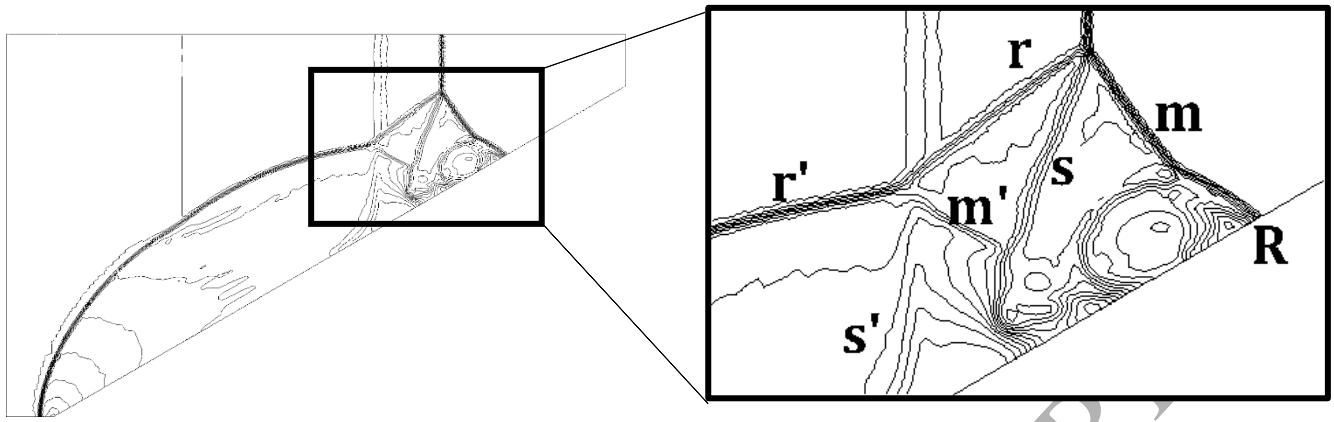

(a) Pure gas

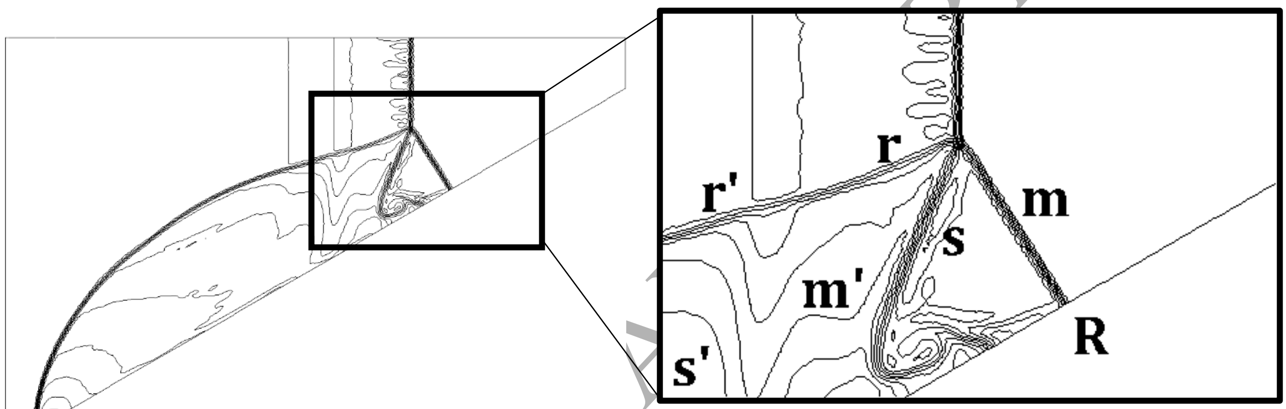

(b) Dusty gas: β=0.1, d=10.0 μm

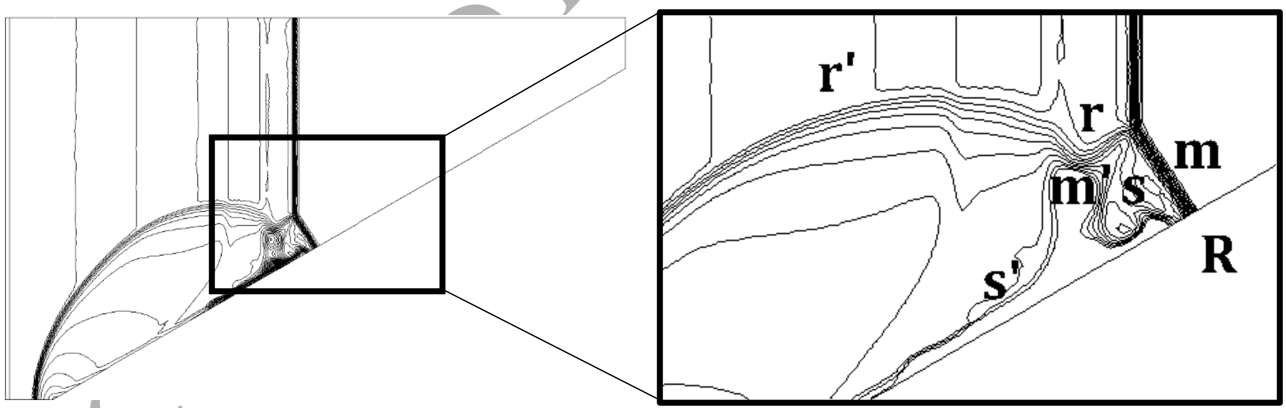

(c) Dusty gas: β=0.5, d=0.5 μm

Fig. 20. Change of the DMR structure in presence of dust particles (P^1 solution)

Another dusty gas case with a particulate loading β=0.5 and a particle diameter 0.5 μm was considered. Such a setting leads to a greater number of particles in the domain compared to the previous case. It can be seen in Fig. 20 (c) that, unlike the previous case in which only the secondary triple point is subject to major change, both the primary and secondary triple points are affected by dust particles. Note also that the incident shock front is significantly decelerated in this case with high dust concentration.

Finally, a more detailed parametric study on the effects of particulate loading and particle diameter size was summarized in Fig. 21. Isopycnic surfaces, that is, surfaces with a constant density of gas phase in the dusty gas indicate that the particulate loading will substantially affect the configuration of the triple points. This change is more significant in the case of larger dust particles. Moreover, when the particulate loading increases, the incident shock front greatly decelerates, especially in the case of smaller dust particles. Furthermore, it can be seen that the height of the Mach stem shortens in dusty gas flows. Due to the increased momentum and thermal interactions, the height of the Mach stem shortens more in the case of a smaller dust particle. In addition, it can be observed that the particle diameter affects the curvature and slope of the secondary and primary reflected shock waves. The larger the particle diameter is the less is the curvature of the secondary reflected wave. Also the primary reflected shock gets more aligned with the secondary reflected shock as the diameter increases. In case of large particles and high mass loadings, the reflected shocks are completely distorted. Furthermore, it can be seen that the slipstreams are affected by increase of particulate loading. The slipstreams are found highly distorted in case of smaller particles. In summary, it can be inferred that the increase of particle diameter and mass loading would lead to blurrier flow patterns of reflected waves and slipstreams. The surfaces of constant density of solid phase in the dusty gas, shown in Fig. 21 (b), imply that smaller particles can follow the gas phase closely, but larger particles cannot follow the gas phase, so

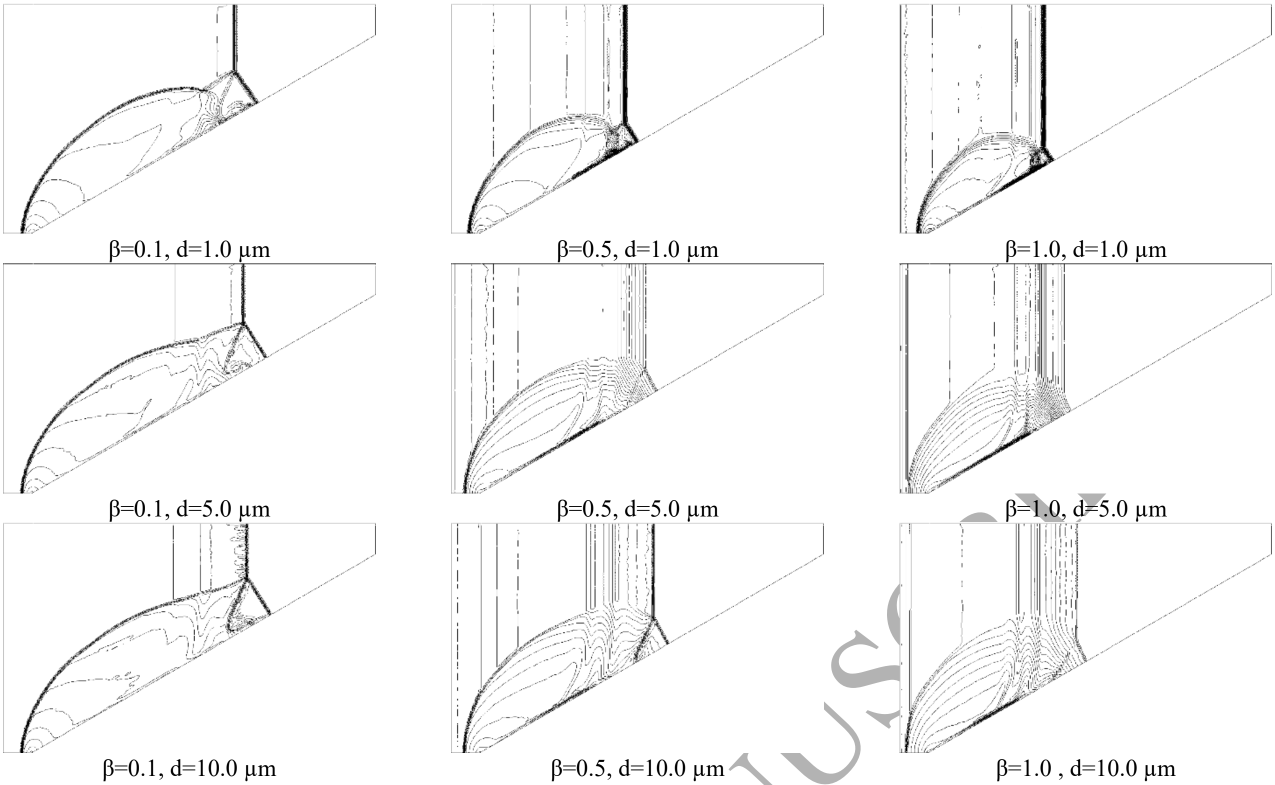

(a) Gas phase

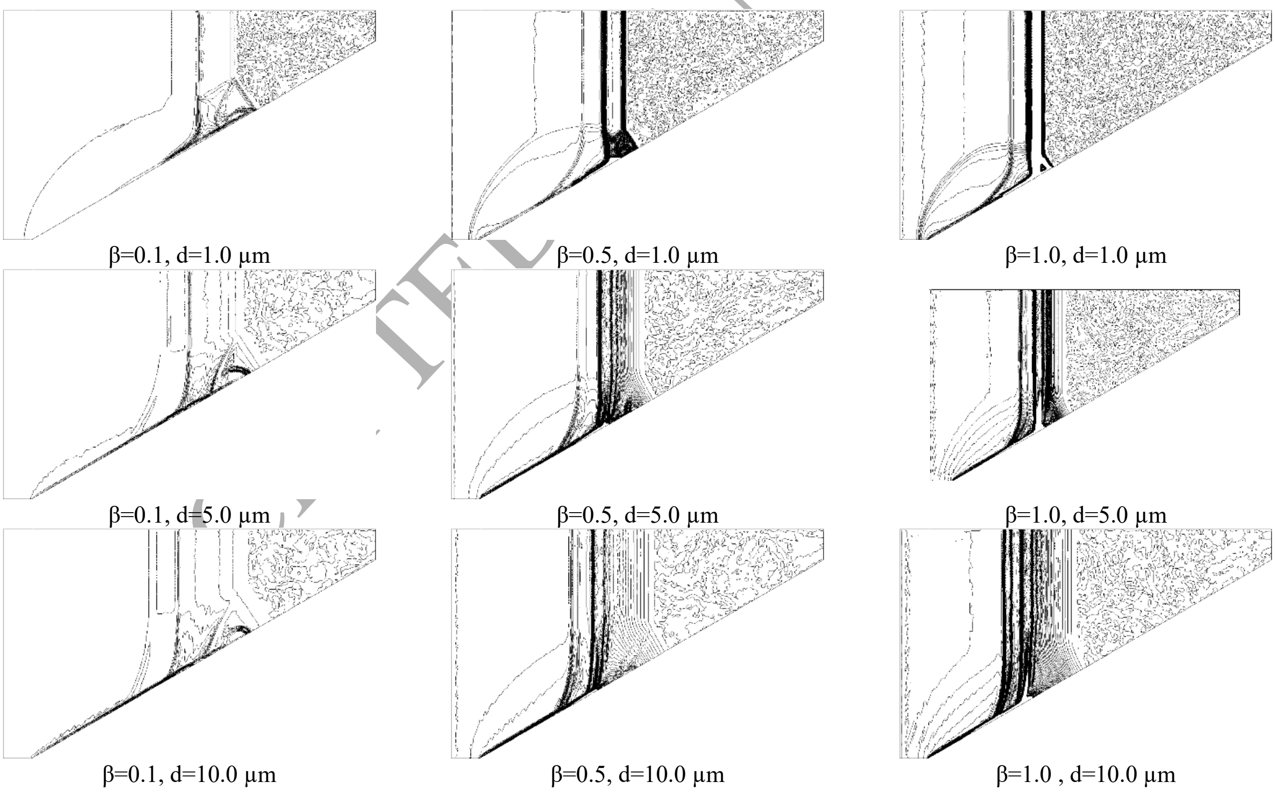

(b) Solid phase

Fig. 21. Parametric study on particulate loading and particle diameter in the double Mach reflection problem (P^1 solution)

that the structure of isopycnic surfaces becomes drastically different from that of the corresponding gas.

4.6. Axisymmetric particle-laden under-expanded jet

One of the few experimental studies on the interaction of particles with shock waves is the case of under-expanded supersonic jets of gas and particle. In this subsection, we investigate the problem of supersonic jets of particle-laden gas (Sommerfeld, 1994). In order to implement the axisymmetric formulation in the present computational framework, the source terms in the system of governing equations should be modified. The axisymmetric equations can be easily derived by following previous studies (Ishii et al., 1989; Pelanti and LeVeque, 2006; Sommerfeld, 1994). The problem is defined as a supersonic jet which is expanded from a high pressure chamber into a low pressure chamber, as illustrated in Fig. 22.

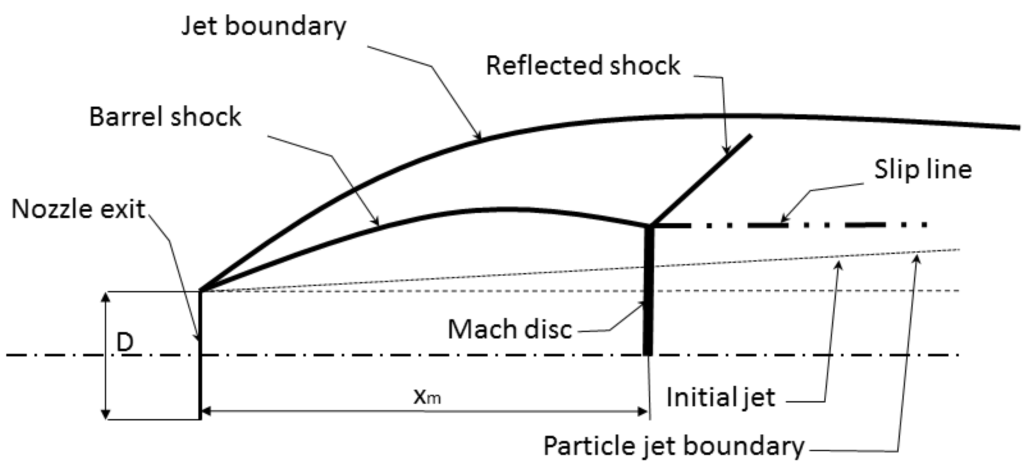

Fig. 22. Schematic of the under-expanded jet of particle-laden gas (computational domain size: 5D×10D)

The location of Mach disk in the absence of particles is first studied for validation of the pure gas solver. This parameter has been experimentally studied by various researchers in the past (Avduevskii et al., 1970; Crist et al., 1966; Lewis and Carlson, 1964; Sommerfeld, 1994). Recently, Franquet et al. (2015) presented an extensive review on experimental works dealing with free under-expanded jets. The comparison of Mach disk location with experimental results is shown in Fig. 23. Generally, the results are in good agreement with experimental data of Avduevskii et al. (1970) for mid-range pressure ratios. In the case of pressure ratios of 2 and 100, our predictions are more close to the experimental results of Lewis and Carlson (1964).

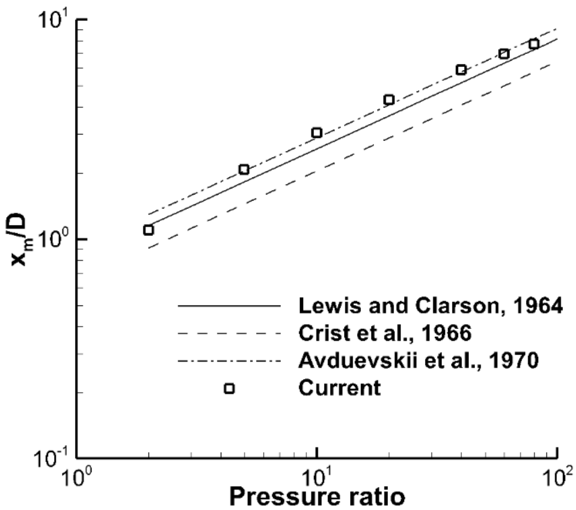

Fig. 23. Comparison of prediction of Mach-disc location depending on the pressure ratio for the pure gas flow with previous experimental results

Moreover, a comparison of dusty gas solutions with experiments of Sommerfeld (1994) is shown in Fig. 24. Here, particle properties are set equal to the values of diameter 45 µm and mass density 2500 kg/m^3. In this problem, one of the important flow features is the upstream movement of Mach disk as a consequence of the interaction of gas phase with particles. As reported in (Sommerfeld, 1994), when the particle loading increases, the Mach disk gets closer to the nozzle exit and the wave patterns observed in the downstream of the Mach disk becomes more pronounced. The phenomena of movement of Mach disk has also been reported in (Carlson and Lewis, 1964) and (Draper and Jarvinen, 1967). As can be seen in Fig.

24 (b), even though an exact match with experimental results is not achieved, a close agreement in the qualitative trend of upstream movement of the Mach disk is found. There were, nonetheless, some differences between the numerical solutions and the experimental shadowgraphs; for example, the curvature of the Mach disk and the width of the jet boundary. While experiments show that the Mach disk tends to straighten as the particle loading increases, the numerical simulation cannot predict this feature. In addition, the width of the jet boundary is over-predicted in the numerical solutions compared to experimental results. Such deviations may arise from the difference in considering the effect of a nozzle. In the present investigation, for the sake of simplicity, the computation is set up to simulate expansion of a circular jet from a hole into ambient condition without considering a nozzle. Apparently, further in-depth investigation will be necessary for capturing all the detailed features observed in experiments.

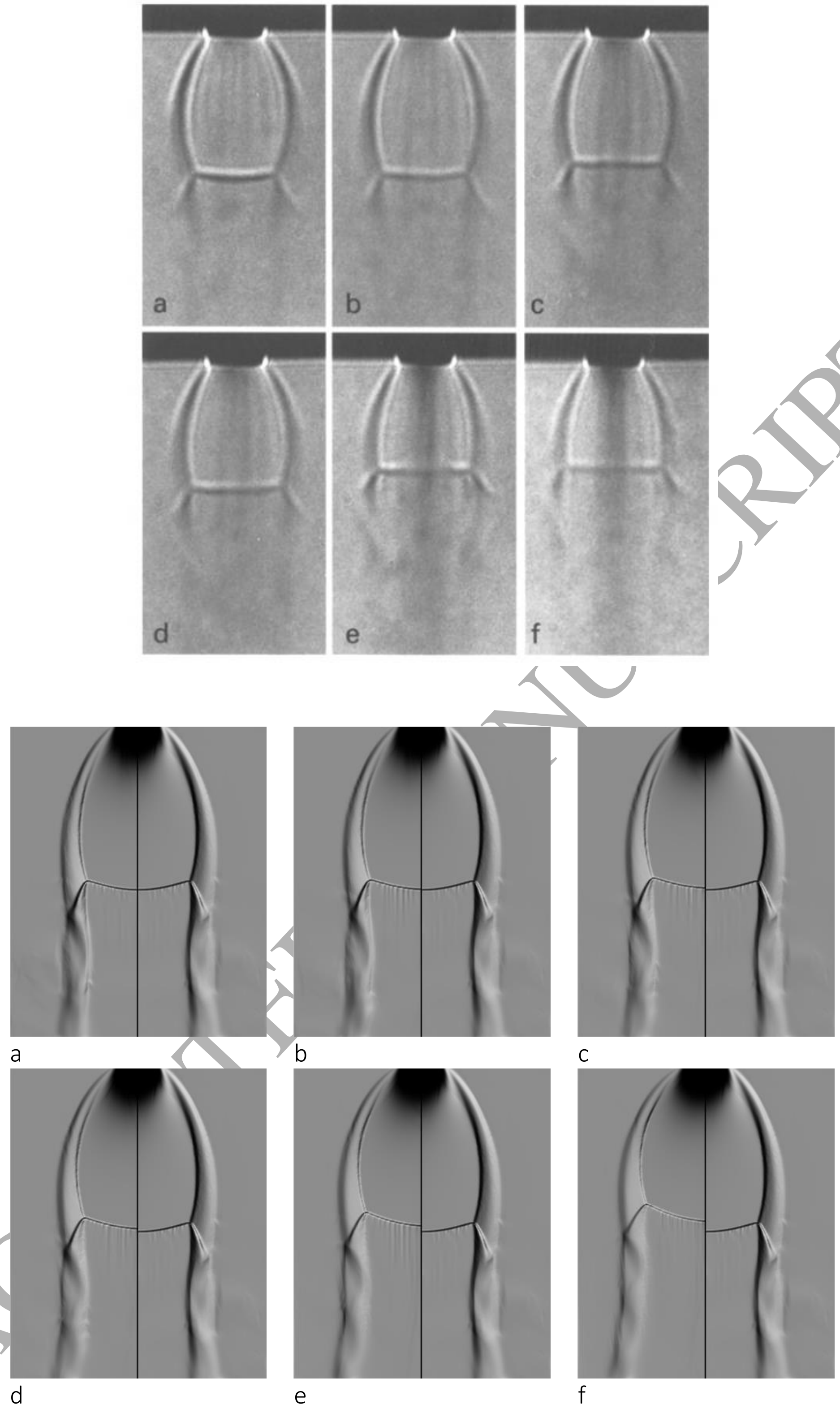

Fig. 24 Shadowgraphs of the under-expanded gas-particle (Sommerfeld, 1994) (top) and density contours of pure gas solution (right) with dusty gas (left) jet for different particle loadings (bottom): **a)** β= 0.0; **b)** β= 0.11 ; **c)** β= 0.24; **d)** β= 0.35; **e)** β= 0.64; **f)** β= 1.07 (P_0 = 0.31MPa, P_0/P_∞ = 29.8, d = 45μm) (P^1 solution)

5. Concluding remarks

Complex wave patterns in dilute gas-particle flows were investigated in detail using a novel DG method developed for solving the two-fluid model for dusty gas flows. In particular, it was shown that, when a dust contact discontinuity is present in the dusty gas flow, a pseudo-compound wave as well as a composite wave can form. Further, the new DG scheme not only meets the demand for high order accuracy (at least second-order) to accurately simulate dusty gas flows, but it can also handle the tricky source terms of coupling effects between the two phases, without resorting to the complicated operator splitting method commonly employed in the conventional method. In fact, in the study of multiphase flow, developing a robust DG solver for dusty gas flows has recently been considered a challenging topic deserving attention.

It turned out that the orthogonality of the basis functions, the backbone of the DG method, again played a critical role in the novel treatment of the high order moments of the polynomial approximations to the source-term. Based on the new DG scheme, various benchmark problems with different physical features in one- and two-dimensional space were studied. In order to elaborate the complex wave patterns in gas-particle flows, the wave propagation mechanisms in the one-dimensional shock tube problem of the dusty gas were first investigated in detail. Several abnormal waves in dusty gas flows—most of them not previously identified—were highlighted and a physical explanation on the origin of such abnormal waves was given.

In addition, the new unstructured DG scheme was applied to two different types of problems with and without the presence of boundary effects. The results in both cases were shown to be in accordance with the previous data. The explosion case was first simulated in such a way that radial symmetry was preserved to confirm the one-dimensional behavior.

Then, the multiphase explosion problem was considered to examine the ability of the numerical method to capture more complex flow patterns. The new scheme was then applied to investigate the compression corner problem for both the single and multi-phase applications. Both single and double Mach reflection problems were solved and the higher order solutions (up to polynomial order of two) were successfully obtained.

Furthermore, a detailed parametric study on particulate loading and particle diameter size was conducted. Isopycnic surfaces indicated that the particulate loading substantially affects the structure of the double Mach reflection, including the configuration of triple points. The main reason for this change is the amplification of the relaxation region, that is, the main element of the abnormal waves in dusty gas flows. In all cases, it was found that the secondary triple point was much more affected by the dust particles. Moreover, the convex Mach stem formed in the pure gas flow changed into a perpendicular Mach stem in the dusty gas flows. It was found that the particle diameter and mass loading affect the slope and curvature of the reflected waves as well. While an increase in particle diameter causes the secondary reflected wave to align along the primary wave, the increase in mass loading leads to increase of the intersection angle of these two waves. It was also found that as the particle diameter and mass loading increase, the structure of the DMR becomes blurrier.

Lastly, based on axisymmetric formulation, the problem of particle-laden free under-expanded jet was investigated for the purpose of validating the numerical simulation in capturing multiphase interactions. Even though a slight over-estimation of Mach disk location and jet boundary width was found in the numerical solutions, the important feature of upstream movement of Mach disk was shown in good agreement with experimental results.

One of the future applications of the present study will be to simulate the impingement of a rocket plume on the lunar surface, and the subsequent dusty gas flows formed by the ejection of solid particles from the regolith. Inherent complexities consisting of various flow regimes—the plume expanding in vacuum, standoff shock, stagnation region, local erosion, supersonic dusty jet flow, rarefied flow, and so on—in this problem will make high-fidelity numerical simulation a grandly challenging problem. We hope to report in future the results of studies of this problem using the present high-resolution DG framework on an Eulerian multiphase system of equations for dusty gas flows.

Acknowledgments

This work was supported by the National Research Foundation of Korea (NRF 2015-M1A3A3A02-010621, 2017-R1A5A1015311), South Korea.

References

Avduevskii, V.S., Ivanov, A., Karpman, I.M., Traskovskii, V.D., Yudelovich, M.Y., 1970. Flow in supersonic viscous under expanded jet. Fluid Dynamics 5, 409-414.

Balachandar, S., Eaton, J.K., 2010. Turbulent dispersed multiphase flow. Annual Review of Fluid Mechanics 42, 111-133.

Barth, T.J., Jespersen, D.C., 1989. The design and application of upwind schemes on unstructured meshes, 27th Aerospace Sciences Meeting. American Institute of Aeronautics and Astronautics.

Ben-Dor, G., Igra, O., Wang, L., 2001. Shock wave reflections in dust-gas suspensions. Journal of fluids engineering 123, 145-153.

Béreux, F., 1996. Zero-relaxation limit versus operator splitting for two-phase fluid flow computations. Computer Methods in Applied Mechanics and Engineering 133, 93-124.

Brennen, C.E., 2005. Fundamentals of Multiphase Flow. Cambridge University Press.

Carcano, S., Bonaventura, L., Esposti Ongaro, T., Neri, A., 2013. A semi-implicit, second-order-accurate numerical model for multiphase underexpanded volcanic jets. Geoscientific Model Development 6, 1905-1924.

Carcano, S., Ongaro, T.E., Bonaventura, L., Neri, A., 2014. Influence of grain-size distribution on the dynamics of underexpanded volcanic jets. Journal of Volcanology and Geothermal Research 285, 60-80.

Carlson, D., Lewis, C., 1964. Normal shock location in underexpanded gas and gas-particle jets. AIAA Journal 2, 776-777.

Cockburn, B., Karniadakis, G.E., Shu, C.W., 2000. The development of discontinuous Galerkin methods, Discontinuous Galerkin Methods. Springer, pp. 3-50.

Cockburn, B., Shu, C.W., 1988. The Runge-Kutta local projection P^1-discontinuous-Galerkin finite element method for scalar conservation laws. Rairo-Modélisation Mathématique et Analyse Numérique 25, 337-361.

Cockburn, B., Shu, C.W., 1989. TVB Runge-Kutta local projection discontinuous Galerkin finite element method for conservation laws. II. General framework. Mathematics of Computation 52, 411-435.

Cockburn, B., Shu, C.W., 1998. The Runge–Kutta discontinuous Galerkin method for conservation laws V: multidimensional systems. Journal of Computational Physics 141, 199-224.

Crist, S., Glass, D., Sherman, P., 1966. Study of the highly underexpanded sonic jet. AIAA journal 4, 68-71.

de Frahan, M.T.H., Varadan, S., Johnsen, E., 2015. A new limiting procedure for discontinuous Galerkin methods applied to compressible multiphase flows with shocks and interfaces. Journal of Computational Physics 280, 489-509.

Deschambault, R., Glass, I., 1983. An update on non-stationary oblique shock-wave reflections: Actual isopycnics and numerical experiments. Journal of Fluid Mechanics 131, 27-57.

Diehl, D., Kremser, J., Kröner, D., Rohde, C., 2016. Numerical solution of Navier–Stokes–Korteweg systems by Local Discontinuous Galerkin methods in multiple space dimensions. Applied Mathematics and Computation 272, 309-335.

Dobran, F., Neri, A., Macedonio, G., 1993. Numerical simulation of collapsing volcanic columns. Journal of Geophysical Research: Solid Earth 98, 4231-4259.

Draper, J., Jarvinen, P., 1967. Underexpanded gas-particle jets. AIAA Journal 5, 824-825.

Dubiner, M., 1991. Spectral methods on triangles and other domains. Journal of Scientific Computing 6, 345-390.

Dumbser, M., Loubère, R., 2016. A simple robust and accurate a posteriori sub-cell finite volume limiter for the discontinuous Galerkin method on unstructured meshes. Journal of Computational Physics 319, 163-199.

Franquet, E., Perrier, V., 2012. Runge–Kutta discontinuous Galerkin method for the approximation of Baer and Nunziato type multiphase models. Journal of Computational Physics 231, 4096-4141.

Franquet, E., Perrier, V., 2013. Runge–Kutta discontinuous Galerkin method for reactive multiphase flows. Computers & Fluids 83, 157-163.

Franquet, E., Perrier, V., Gibout, S., Bruel, P., 2015. Free underexpanded jets in a quiescent medium: a review. Progress in Aerospace Sciences 77, 25-53.

Gosse, L., 2000. A well-balanced flux-vector splitting scheme designed for hyperbolic systems of conservation laws with source terms. Computers & Mathematics with Applications 39, 135-159.

Gurris, M., Kuzmin, D., Turek, S., 2010. Finite element simulation of compressible particle-laden gas flows. Journal of Computational and Applied Mathematics 233, 3121-3129.

Igra, O., Ben-Dor, G., Rakib, Z., 1985. The effect of dust and water droplets on the relaxation zone developed behind strong normal shock waves. International Journal of Multiphase Flow 11, 121-132.

Igra, O., Elperin, I., Ben-Dor, G., 1999. Dusty gas flow in a converging-diverging nozzle. Journal of Fluids Engineering 121, 908-913.

Igra, O., Hu, G., Falcovitz, J., Wang, B., 2004. Shock wave reflection from a wedge in a dusty gas. International Journal of Multiphase Flow 30, 1139-1169.

Ishii, R., Umeda, Y., Yuhi, M., 1989. Numerical analysis of gas-particle two-phase flows. Journal of fluid mechanics 203, 475-515.

Jacobs, G.B., Don, W.S., 2009. A high-order WENO-Z finite difference based particle-source-in-cell method for computation of particle-laden flows with shocks. Journal of Computational Physics 228, 1365-1379.

Karniadakis, G., Sherwin, S., 2013. Spectral/hp Element Methods for Computational Fluid Dynamics. Oxford University Press.

Kim, S.W., Chang, K.S., 1991. Reflection of shock wave from a compression corner in a particle-laden gas region. Shock Waves 1, 65-73.

Klieber, W., Rivière, B., 2006. Adaptive simulations of two-phase flow by discontinuous Galerkin methods. Computer Methods in Applied Mechanics and Engineering 196, 404-419.

Knudsen, J.G., Katz, D.L., 1958. Fluid dynamics and heat transfer.

Kontzialis, K., Ekaterinaris, J.A., 2013. High order discontinuous Galerkin discretizations with a new limiting approach and positivity preservation for strong moving shocks. Computers & Fluids 71, 98-112.

Kührt, E., Keller, H., 1996. On the importance of dust in cometary nuclei. Earth, Moon, and Planets 72, 79-89.

LeVeque, R.J., Yee, H.C., 1990. A study of numerical methods for hyperbolic conservation laws with stiff source terms. Journal of Computational Physics 86, 187-210.

Levine, A.S., 1971. A theoretical analysis of unsteady supersonic, gas-particle suspension flows using the particle-in-cell method. Northeastern University.

Lewis, C., Carlson, D., 1964. Normal shock location in underexpanded gas and gas-particle jets. AIAA Journal 2, 776-777.

Li, H., Ben-Dor, G., 1999. Analysis of double-Mach-reflection wave configurations with convexly curved Mach stems. Shock Waves 9, 319-326.

Lock, G., 1994. Experimental measurements in a dusty-gas shock tube. International Journal of Multiphase Flow 20, 81-98.

Lu, H., Zhu, J., Wang, D., Zhao, N., 2016. Runge–Kutta discontinuous Galerkin method with front tracking method for solving the compressible two-medium flow. Computers & Fluids 126, 1-11.

Lucier, B.J., 1985. Error bounds for the methods of Glimm, Godunov and LeVeque. Siam Journal on Numerical Analysis 22, 1074-1081.

Marble, F.E., 1970. Dynamics of dusty gases. Annual Review of Fluid Mechanics 2, 397-446.

McFarland, J.A., Black, W.J., Dahal, J., Morgan, B.E., 2016. Computational study of the shock driven instability of a multiphase particle-gas system. Physics of Fluids 28, 024105.

Metzger, P.T., Smith, J., Lane, J.E., 2011. Phenomenology of soil erosion due to rocket exhaust on the Moon and the Mauna Kea lunar test site. Journal of Geophysical Research: Planets 116.

Miura, H., Glass, I.I., 1982. On a dusty-gas shock tube, Proceedings of the Royal Society of London A: Mathematical, Physical and Engineering Sciences. The Royal Society, pp. 373-388.

Moortgat, J., Firoozabadi, A., 2016. Mixed-hybrid and vertex-discontinuous-Galerkin finite element modeling of multiphase compositional flow on 3D unstructured grids. Journal of Computational Physics 315, 476-500.

Myong, R.S., Roe, P.L., 1997. Shock waves and rarefaction waves in magnetohydrodynamics. Part 2. The MHD system. Journal of Plasma Physics 58, 521-552.

Owkes, M., Desjardins, O., 2013. A discontinuous Galerkin conservative level set scheme for interface capturing in multiphase flows. Journal of Computational Physics 249, 275-302.

Pelanti, M., LeVeque, R.J., 2006. High-resolution finite volume methods for dusty gas jets and plumes. SIAM Journal on Scientific Computing 28, 1335-1360.

Perot, J.B., 1993. An analysis of the fractional step method. Journal of Computational Physics 108, 51-58.

Popel, S., Gisko, A., 2006. Charged dust and shock phenomena in the solar system. Nonlinear Processes in Geophysics 13, 223-229.

Qiu, J., Khoo, B.C., Shu, C.W., 2006. A numerical study for the performance of the Runge–Kutta discontinuous Galerkin method based on different numerical fluxes. Journal of Computational Physics 212, 540-565.

Reed, W.H., Hill, T., 1973. Triangular mesh methods for the neutron transport equation. Los Alamos Report LA-UR-73-479.

Rudinger, G., 1964. Some properties of shock relaxation in gas flows carrying small particles. Physics of Fluids 7, 658-663.

Sainsaulieu, L., 1995. Finite volume approximation of two phase-fluid flows based on an approximate Roe-type Riemann solver. Journal of Computational Physics 121, 1-28.

Saito, T., 2002. Numerical analysis of dusty-gas flows. Journal of Computational Physics 176, 129-144.

Saito, T., Glass, I.I., 1984. Application of random-choice method to problems in gasdynamics. Progress in Aerospace Sciences 21, 201-247.

Saito, T., Marumoto, M., Takayama, K., 2003. Numerical investigations of shock waves in gas-particle mixtures. Shock Waves 13, 299-322.

Sapko, M.J., Weiss, E.S., Cashdollar, K.L., Zlochower, I.A., 2000. Experimental mine and laboratory dust explosion research at NIOSH. Journal of Loss Prevention in the Process Industries 13, 229-242.

Satofuka, N., Tokita, K., 1979. Finite difference calculation of gas-particle flows in shock tubes. Mem. Fac. Ind. Arts, Kyoto Techn. Univ 28, 28-39.

Saurel, R., Daniel, E., Loraud, J.C., 1994. Two-phase flows: Second-order schemes and boundary conditions. AIAA Journal 32, 1214-1221.

Sommerfeld, M., 1985. The unsteadiness of shock waves propagating through gas-particle mixtures. Experiments in Fluids 3, 197-206.

Sommerfeld, M., 1994. The structure of particle-laden, underexpanded free jets. Shock waves 3, 299-311.

Tiselj, I., Petelin, S., 1997. Modelling of two-phase flow with second-order accurate scheme. Journal of Computational Physics 136, 503-521.

Toro, E.F., 2013. Riemann Solvers and Numerical Methods for Fluid Dynamics: a Practical Introduction. Springer Science & Business Media.

Tosh, A., Liever, P.A., Arslanbekov, R.R., Habchi, S.D., 2011. Numerical analysis of spacecraft rocket plume impingement under lunar environment. Journal of Spacecraft and Rockets 48, 93-102.

Toumi, I., Kumbaro, A., 1996. An approximate linearized Riemann solver for a two-fluid model. Journal of Computational Physics 124, 286-300.

Vié, A., Pouransari, H., Zamansky, R., Mani, A., 2016. Particle-laden flows forced by the disperse phase: Comparison between Lagrangian and Eulerian simulations. International Journal of Multiphase Flow 79, 144-158.

Volkov, A., Tsirkunov, Y.M., Oesterle, B., 2005. Numerical simulation of a supersonic gas–solid flow over a blunt body: The role of inter-particle collisions and two-way coupling effects. International Journal of Multiphase Flow 31, 1244-1275.

Walker, G.P., 1981. Generation and dispersal of fine ash and dust by volcanic eruptions. Journal of Volcanology and Geothermal Research 11, 81-92.

Wan, G., Sun, G., Xue, X., Shi, M., 2008. Solids concentration simulation of different size particles in a cyclone separator. Powder Technology 183, 94-104.

Wang, C., Zhang, X., Shu, C.W., Ning, J., 2012. Robust high order discontinuous Galerkin schemes for two-dimensional gaseous detonations. Journal of Computational Physics 231, 653-665.

Woodward, P., Colella, P., 1984. The numerical simulation of two-dimensional fluid flow with strong shocks. Journal of Computational Physics 54, 115-173.

Zhang, X., Shu, C.W., 2010a. On maximum-principle-satisfying high order schemes for scalar conservation laws. Journal of Computational Physics 229, 3091-3120.

Zhang, X., Shu, C.W., 2010b. On positivity-preserving high order discontinuous Galerkin schemes for compressible Euler equations on rectangular meshes. Journal of Computational Physics 229, 8918-8934.

Zhang, X., Shu, C.W., 2011. Positivity-preserving high order discontinuous Galerkin schemes for compressible Euler equations with source terms. Journal of Computational Physics 230, 1238-1248.